

# SFFT-based Homogenization: Using Tensor Trains to Enhance FFT-Based Homogenization

Sascha H. Hauck<sup>1, 2\*</sup>, Matthias Kabel<sup>1\*</sup>, Mazen Ali<sup>1, 3\*</sup>, and Nicolas R. Gauger<sup>2\*</sup>

<sup>1</sup>*Department of Flow and Material Simulation, Fraunhofer ITWM, Kaiserslautern, 67663 Germany;*

<sup>2</sup>*Chair for Scientific Computing, University of Kaiserslautern-Landau (RPTU), 67663 Germany;*

<sup>3</sup>*Multiverse Computing, Paseo de Miramón, E-20014 San Sebastián, Spain*

---

Homogenization is a key technique for approximating the macroscopic properties of materials with microscale heterogeneity. The FFT-based Homogenization method has gained widespread usage due to its computational efficiency and accuracy in handling complex microstructures. However, despite its advantages, the method is limited by speed and memory constraints, particularly when applied to high-resolution discretizations. These limitations affect its scalability and efficiency, especially in large-scale simulations or when dealing with highly detailed microstructures. These challenges arise from the fundamental reliance on the Fast Fourier Transform, which imposes inherent restrictions on further advancements.

In this paper, we propose a novel SFFT-based Homogenization algorithm that utilizes a Quantized Tensor Train variant of the Quantum Fourier Transform. This method is tailored to the geometry under consideration and offers significant improvements in time complexity and memory efficiency compared to the traditional FFT-based approach while remaining executable on classical hardware. The method is applicable only if a suitable Quantized Tensor Train representation exists for the stiffness operator associated with the underlying geometry.

**Homogenization, Tensor Networks, Tensor Trains, Quantum Computing, Superfast Fourier Transform**

## 1 Introduction

Homogenization is a mathematical technique used to approximate the macroscopic properties of materials with microscale heterogeneity, such as composites and alloys [1-3]. Computational Homogenization enables simulations of such materials, even when microstructural features are orders of magnitude smaller than the macroscopic scale [4].

One of the most prominent numerical techniques is the FFT-based Homogenization, widely recognized for its efficiency and accuracy in handling complex microstructures. Developed by Moulinec and Suquet in 1998 [5], this approach offers significant advantages over traditional finite element methods (FEM) [6]. By bypassing the computationally expensive process of assembling local stiffness matrices required in FEM, the FFT-based method leverages the Fast Fourier Transform (FFT) to iteratively solve the Lippmann-Schwinger equation, thereby obtaining the macroscopic stiffness tensor [7-9].

In recent years, several approaches have sought to improve state-of-the-art FFT-based Homogenization methods. One such strategy explores the use of quantum com-

puting, specifically by utilizing the improved time complexity of the Quantum Fourier Transform (QFT) over the traditional FFT [10,11]. While these approaches are promising, they face significant challenges due to the need for fault-tolerant quantum computing. As a result, these methods are unlikely to be feasible in the near future, particularly within the current Noisy Intermediate-Scale Quantum (NISQ) era.

Another promising approach employs tensor networks (TNs) in a 'quantum-inspired' manner, aiming to achieve computational speedups through compression. Although these methods do not face the same challenges as quantum computing, they still fall short in overcoming the time complexity barrier imposed by the FFT [12,13].

Recently, Chen et al. [14] demonstrated that the previously unsuccessful attempt to transfer the QFT into a low-rank tensor network could be accomplished with minor modifications to the original QFT quantum circuit. The resulting tensor network operator was an adaptation of the Superfast Fourier Transform (SFFT), originally introduced by Dolgov et al. in 2012 [15]. This adap-

tation showed significantly improved speed compared to the FFT, provided the data exhibited favourable structural properties.

In this paper, we present a novel SFFT-based Homogenization algorithm and investigate its applicability to various geometries in both 2D and 3D. A key aspect of our analysis is the memory consumption and speed of our approach, which we compare to the state-of-the-art FFT-based Homogenization method. Our goal is to achieve scalability similar to the QFT while ensuring practical computability with classical computers.

The outline of the remainder of this paper is as follows: Section 2 presents the derivation of the FFT-based Homogenization algorithm and discusses its limitations, while Section 3 introduces the (Quantized) Tensor Train format. Section 4 presents the 'Zip-Up' algorithm, which converts our QFT quantum circuit into the desired SFFT Tensor Train, and concludes with our novel SFFT-based Homogenization algorithm. In Section 5, we compare the performance of our approach to the state-of-the-art FFT-based Homogenization method, focusing primarily on speed and memory consumption. Before closing, we provide a short summary of the paper – along with the statement of the main conclusions drawn – in Section 6.

## 2 FFT-based Homogenization

The primary objective of the FFT-based Homogenization is to determine the effective linearly elastic macroscopic stiffness tensor  $\mathbf{C}^{\text{eff}}$  of a composite, assuming the properties of the individual constituents are known. The stiffness tensor  $\mathbf{C}^{\text{eff}}$  is defined through the macroscopic stress-strain relationship

$$\sigma^{\text{eff}} = \mathbf{C}^{\text{eff}} \mathbf{E}, \quad (1)$$

where  $\sigma^{\text{eff}}$  and  $\mathbf{E}$  represent the macroscopic stress and strain tensors, respectively.

To solve the above equation, it is advantageous to perform the analysis at the local scale of the heterogeneities in the composite. Within this region, a representative volume element (RVE)  $\mathcal{V}$  is defined, which is assumed to be significantly smaller than the overall material length scale [16]. This approach, where a macroscopic problem is addressed by first solving a microscopic problem on an RVE, is referred to as the Corrector problem [17].

In this setting, assuming periodic boundary conditions on the RVE, the local strain field can be written as

$$\varepsilon(\mathbf{x}) = \mathbf{E} + \nabla^{\text{S}} \mathbf{u}(\mathbf{x}), \quad (2)$$

where  $\nabla^{\text{S}}$  and  $\mathbf{u}(\mathbf{x})$  are the symmetrized nabla-operator

and the local displacement field, respectively. By imposing the condition of a vanishing average

$$\frac{1}{|\mathcal{V}|} \int_{\mathcal{V}} \nabla \mathbf{u}(\mathbf{x}) d\mathbf{x} = 0,$$

it is assured that the macroscopic strain  $\mathbf{E}$  represents the mean strain over the RVE. Since the macroscopic strain is assumed to be known, the focus of the derivation shifts to finding a representation of the fluctuation term  $\nabla^{\text{S}} \mathbf{u}(\mathbf{x})$ .

We continue the derivation by identifying that the local stress tensor must satisfy the force-equilibrium equation

$$\begin{aligned} \text{div } \sigma(\mathbf{x}) &= \text{div} \{ \mathbf{C}(\mathbf{x}) [\mathbf{E} + \nabla^{\text{S}} \mathbf{u}(\mathbf{x})] \} \\ &= 0. \end{aligned} \quad (3)$$

To address the local problem, equation (3) is reformulated through an isotropic reference material, characterized by a constant stiffness tensor  $\mathbf{C}_0$  [17], leading to

$$\text{div} \{ \mathbf{C}_0 [\mathbf{E} + \nabla^{\text{S}} \mathbf{u}(\mathbf{x})] + \tau(\mathbf{x}) \} = 0. \quad (4)$$

with the polarization tensor

$$\tau(\mathbf{x}) = [\mathbf{C}(\mathbf{x}) - \mathbf{C}_0] [\mathbf{E} + \nabla^{\text{S}} \mathbf{u}(\mathbf{x})]. \quad (5)$$

The closed-form differential equation (4) can be solved using a Green's function  $G_0$ , resulting in the following expression for the displacement gradient

$$\nabla^{\text{S}} \mathbf{u}(\mathbf{x}) = -(\Gamma_0 \star \tau)(\mathbf{x}), \quad (6)$$

where  $\Gamma_0 = \varepsilon G_0 \text{div}$  denotes the Green-Eshelby Operator for strains [18]. It is important to note that the divergence operator  $\text{div}$  plays a crucial role in defining the discretization scheme used [19], see Appendix A for a detailed discussion. By substituting the solution (6) into the strain expression (2), and applying the definition of the polarization tensor (5), we obtain the Lippmann-Schwinger equation

$$\varepsilon(\mathbf{x}) = \mathbf{E} - \{ \Gamma_0 \star [(\mathbf{C} - \mathbf{C}_0) \varepsilon] \}(\mathbf{x}). \quad (7)$$

However, since the Green-Eshelby Operator has a known analytical form in Fourier space, equation (6) can be transformed accordingly, yielding

$$\mathcal{F}[\nabla \mathbf{u}](\mathbf{q}) = -\hat{\Gamma}_0(\mathbf{q}) \hat{\tau}(\mathbf{q}), \quad (8)$$

where the Fast Fourier Transform (FFT)  $\mathcal{F}[\cdot]$  is employed for efficient computation. Throughout this paper, variables in momentum space will be denoted by a hat symbol to distinguish them from their real-space counterparts.

Finally, the FFT-based Homogenization algorithm 1 is derived by incorporating the Fourier representation of the Green-Eshelby Operator (8) into the

Lippmann-Schwinger equation (7). The algorithm iteratively refines the initial approximation of the local strain, conveniently initialized as the mean strain  $\mathbf{E}$ , by accounting for local variations in the material structure. The iterations continue until a predefined accuracy threshold  $\delta_{\text{tol}}$  is achieved.

---

**Algorithm 1:** FFT-based Homogenization Algorithm

---

**Input:** Mean strain field  $\varepsilon_0 = \mathbf{E}$

**while** *not converged* **do**

```

     $\tau_m = (\mathbf{C} - \mathbf{C}_0) \varepsilon_m$ 
     $\hat{\tau}_m = \mathcal{F}[\tau_m]$ 
     $\hat{\varepsilon}_m = \hat{I}_0 \hat{\tau}_m$ 
     $\varepsilon_{m+1} = \mathbf{E} - \mathcal{F}^{-1}[\hat{\varepsilon}_m]$ 
     $m = m + 1$ 
    if  $\|\frac{\varepsilon_{m+1} - \varepsilon_m}{\mathbf{E}}\| < \delta_{\text{tol}}$  then
        | break;
    end

```

**end**

**Return:** Local strain field  $\varepsilon_{m+1}$

---

Working with tensor representations can often be cumbersome, both in terms of clarity and computational efficiency. To address this, we adopt Voigt notation, which represents stress and strain tensors as 3 (6) dimensional vectors in this notation, the stiffness tensor is represented as a  $3 \times 3$  ( $6 \times 6$ ) matrix acting on them in 2 (3) dimensional space. This reduction is made possible by exploiting the inherent symmetries of the tensors [20].

The effective stiffness tensor  $\mathbf{C}^{\text{eff}}$  can conveniently be determined in Voigt notation, where the strain-stress relationship (1) reduces to a simple matrix-vector product. By selectively controlling the mean strain  $\mathbf{E}$  - where only its  $k$ -th component to unity while all others are set to zero - the relationship simplifies to its component form

$$\sigma_i^{\text{eff}} = \mathbf{C}_{ij}^{\text{eff}} \delta_{jk} = \mathbf{C}_{ik}^{\text{eff}}.$$

Using this approach, the  $k$ -th column of the effective stiffness matrix can be computed directly from the macroscopic stress vector  $\sigma^{\text{eff}}$ . Consequently, by successively setting the mean strain components to unity, the columns of the effective stiffness matrix can be systematically determined. Additionally, the specified mean strains are provided as input to Algorithm 1. The algorithm's output is then used to compute the macroscopic stress vectors  $\sigma^{\text{eff}}$  by averaging over the RVE

$$\sigma^{\text{eff}} = \frac{1}{|\mathcal{V}|} \int_{\mathcal{V}} \sigma_m(\mathbf{x}) d\mathbf{x} = \frac{1}{|\mathcal{V}|} \int_{\mathcal{V}} \mathbf{C}(\mathbf{x}) \varepsilon_m(\mathbf{x}) d\mathbf{x}.$$

This approach allows for the complete computation of the effective stiffness matrix  $\mathbf{C}^{\text{eff}}$ .

We conclude this section by noting that the computational complexity of the FFT-based algorithm 1

is dominated by the FFT operations, scaling with  $\mathcal{O}(N^D \log N)$ , where  $N$  is the number of discretization points per dimension  $D$ . Thus, improving the FFT-based Homogenization procedure relies on either enhancing the performance of FFT operations, such as through hardware acceleration, or circumventing the classical FFT entirely.

### 3 Tensor Train Methods

Tensor Networks (TNs) have a rich and diverse history, having been developed independently within both the mathematics and physics communities [22, 23]. This cross-disciplinary development led to a variety of powerful and complementary approaches across the field. In the context of TNs, high-order tensors are decomposed into a network of lower-order tensors, interconnected through specific contraction patterns. This allows for efficient manipulation and representation of complex data.

There are various TN formats, including Tree Tensor Networks (TTNs) and Projected Entangled Pair States (PEPS) [22, 24, 25]. These methods are well-suited for representing and processing high-dimensional tensors, with each having its own advantages in different contexts. However, this work specifically focuses on the Tensor Train (TT) format, along with some of its special cases, for representing high-order tensors  $\mathcal{T}$  [26, 27].

The elements of  $\mathcal{T}$  are related to its TT decomposition as follows

$$\mathcal{T}(i_1, \dots, i_n) = \sum_{\alpha_k} C_{\alpha_0}^{\alpha_1}(i_1) C_{\alpha_1}^{\alpha_2}(i_2) \dots C_{\alpha_{n-1}}^{\alpha_n}(i_n), \quad (9)$$

where each physical index  $i_k$  runs from 0 to  $d_k - 1$ . The novel 3-order tensors  $C_{\alpha_{k-1}}^{\alpha_k}(i_k)$  of shape  $(r_k \times d_k \times r_{k-1})$  are regarded as the cores of the TT. The highest dimensionality of all the virtual subspaces is denoted as the rank  $r$  of the TT providing insight into the feasibility of employing TTs.

The primary advantage of TNs over full tensor representations lies in their data compression capabilities. An  $n$ -order tensor, with each index having a dimension of  $d$ , requires exponential memory  $\mathcal{O}(d^n)$  to store its data. In contrast, the same tensor in the TT format scales linearly with its dimension and order  $\mathcal{O}(ndr^2)$ , while now additionally depending on its rank. Thus, effective compression is achieved only if the rank  $r$  remains moderate.

The feasibility of the TT decomposition relies on the underlying structure of the tensor. Unstructured tensors, such as random tensors, do not have a low-rank representation and are therefore unsuitable for TT decomposition. This limitation is not specific to TT but applies generally to TNs. However, different TN formats

may represent the same structured data in various ways, resulting in varying levels of compression efficiency [28].

Moreover, TTs are not merely a means of compressed storage. They offer a robust mathematical framework that enables efficient operations, leading to significant computational speedups when applicable. The extent of this acceleration depends primarily on the TT rank. The time complexity and rank evolution of TTs under basic linear algebra are summarized in Table 3. Given the broad mathematical foundation of TTs, we refer readers to I. V. Oseledets introduction instead of discussing basic linear algebra in detail [29].

A generalization called the Tensor Train Operator (TTO), can be obtained by extending the TT formula 9 to include an additional physical index per core

$$\begin{aligned} \tilde{T}(\{i_1, j_1\}, \dots, \{i_n, j_n\}) &= \sum_{\alpha_k} G_{\alpha_0}^{\tilde{\alpha}_1}(i_1, j_1) G_{\alpha_0}^{\tilde{\alpha}_1}(i_1, j_1) \dots \\ &\quad \times G_{\alpha_{n-1}}^{\tilde{\alpha}_n}(i_n, j_n). \end{aligned} \quad (10)$$

The physical index pairs of each core can be interpreted as incoming and outgoing dimensions, which allows a TT to be contracted with a TTO. Therefore, the TTO acts as a complex transformation on a TT.

A more complex class of operations includes optimization algorithms, often employed to solve linear systems of equations (LSE). In this paper, we discuss an adaptation of the alternating minimal energy (AMEn) algorithm [30]. Rather than using the AMEn algorithm to solve LSEs, we modify it to accelerate matrix-vector product calculations by adjusting the loss function in the optimization process. Our goal is to find an approximate solution  $v$  of the equation  $Au = \tilde{v}$ , with the exact TTs  $u$  and  $\tilde{v}$  by minimising the following cost function

$$\begin{aligned} L(\tilde{v}) &= \|v - \tilde{v}\|^2 \\ &= (v, \tilde{v}) - 2\Re(Au, v) + const. \end{aligned}$$

The general procedure closely follows the derivation outlined in Dolgov’s work [30], with deviations in certain

details. Additional information on the adapted method is provided in Appendix B.

The primary advantage of this class of optimization methods over direct TTO-TT contractions becomes evident in the high-rank regime. The introduced approach not only reduces time complexity but also results in lower final ranks, often eliminating the need for an additional TT rounding step. As shown in Table 3, this speeds up subsequent operations.

To contract tensors efficiently, it can be beneficial to represent a regular TT as a TTO to perform computations. This is mainly due to the enhanced efficiency of the corresponding optimization methods. Assume we have a TT  $u$  as defined by equation (9). We can raise it to a TTO  $U$ , following the format in equation (10), by employing delta functions

$$G_{\alpha_{k-1}}^{\alpha_k}(i_k, j_k) = C_{\alpha_{k-1}}^{\alpha_k}(i_k) \delta(i_k, j_k), \quad (11)$$

where the novel TTO cores  $G_{\alpha_{k-1}}^{\alpha_k}(i_k, j_k)$  are 4-order tensors of shape  $(d_k \times r_k \times d_k \times r_{k-1})$ . The TTO derived from relation (11) applied to a TT  $v$  produces the same outcome as the Hadamard product of  $u$  and  $v$ . However, the rank of the resulting TT exhibits enhanced scalability, as it is no longer governed by the product of the ranks of  $u$  and  $v$ , see Table 3. A detailed proof is provided in Appendix C.

In general, operations increase the rank when applied on a TT, eventually becoming computationally intractable, as shown in Table 3. To address this issue, additional rounding operations must be employed. Given a tensor  $v$  in TT format, the goal is to find an approximation  $\tilde{v}$  such that

$$\|v - \tilde{v}\|_F \leq \delta_{\text{acc}} \|v\|_F, \quad (12)$$

fulfilling the desired accuracy  $\delta_{\text{acc}}$  in terms of the Frobenius norm  $\|\cdot\|_F$ . The process involves sequential orthogonalization of TT cores followed by truncated SVDs, cutting small singular values. To reach the desired accuracy, the truncation threshold during the procedure

**Table 3** Rank Growth and Time Complexity for Different TT Operations (adapted from Kornev et al. [21]).

| Operations                                 | Rank Result          | Time Complexity                  |
|--|----------------------|----------------------------------|
| $z = x * const$                            | $r(z) = r(x)$        | $\mathcal{O}(dr(x))$             |
| $z = x + y$                                | $r(z) = r(x) + r(y)$ | $\mathcal{O}(nd[r(x) + r(y)]^2)$ |
| $z = xy$                                   | $r(z) = r(x) * r(y)$ | $\mathcal{O}(ndr^3(x)r^3(y))$    |
| $z = Ax$ (contract)                        | $r(z) = r(x) * r(A)$ | $\mathcal{O}(ndr^3(A)r^3(x))$    |
| $z = Ax$ (solve $z$ )                      | $r(z)$               | $\mathcal{O}(ndr(A)r^3(z))$      |
| $Az = x$ (solve $z$ )                      | $r(z)$               | $\mathcal{O}(ndr(A)r^3(z))$      |
| $z = \text{round}(x, \delta_{\text{acc}})$ | $r(z) \leq r(x)$     | $\mathcal{O}(ndr^3(x))$          |

must satisfy the condition

$$\delta_{\text{trunc}} = \frac{\delta_{\text{acc}}}{\sqrt{1-n}}.$$

This iterative process preserves essential information while maintaining a reduced rank and computational tractability [29].

## 4 Quantum-Inspired Approach

To align the TT format with quantum circuits, we restrict the dimensionality of the physical indices to  $d = 2$ . This specialization, called the Quantized Tensor Train (QTT) format, directly links the core dimensionality to the single-qubit subspaces in quantum circuits. Thus, an  $n$ -core QTT represents an  $n$ -qubit quantum state, with unitary gates acting on these qubits being represented as Quantized Tensor Train Operators (QTTOs).

The mathematical relationship between the QTT format and quantum circuits reveals a closeness in both their mathematical structure and diagrammatic representations. This duality forms the cornerstone of our quantum-inspired approach.

### 4.1 The Quantum Fourier Transform

The QFT results from a quantum circuit implementation of the classical FFT through the use of Hadamard  $H$ , (controlled  $c$ ) Phase  $P(\theta)$  and  $SWAP$  Gates acting on either single or neighbouring qubit pairs

$$H = \frac{1}{\sqrt{2}} \begin{pmatrix} 1 & 1 \\ 1 & -1 \end{pmatrix}, \quad SWAP = \begin{pmatrix} 1 & 0 & 0 & 0 \\ 0 & 0 & 1 & 0 \\ 0 & 1 & 0 & 0 \\ 0 & 0 & 0 & 1 \end{pmatrix},$$

$$P(\theta) = \begin{pmatrix} 1 & 0 \\ 0 & e^{i\theta} \end{pmatrix}, \quad cP(\theta) = \begin{pmatrix} 1 & 0 & 0 & 0 \\ 0 & 1 & 0 & 0 \\ 0 & 0 & 1 & 0 \\ 0 & 0 & 0 & e^{i\theta} \end{pmatrix}.$$

The complete circuit is shown in Figure 1. Alternatively, the QFT can be written as a product of two operators  $QFT_n = R_n Q_n$ . The  $Q_n$  circuit is generally responsible for the transformation itself, while the  $R_n$  contribution reorders the output through a succession of  $SWAP$  Gates. The latter one is needed to achieve the same ordering convention as is used within its classical counterpart.

The QFT exhibits an exponentially improved time complexity of  $\mathcal{O}(d \log(N)^2)$  compared to the regular FFT, which scales as  $\mathcal{O}(N^d \log(N))$ , making it a desirable alternative.

The transfer of the QFT into its corresponding QTT formulation has been done previously, however, it was deemed impractical due to its high ranks [15, 31]. Recently, Chen et al. [14] showed that this may be true for the full QFT, but not for its reduced form  $Q_n$ . Specifically, they showed that when the reordering operator  $\mathcal{R}_n$  is not considered, the ranks obtained for the QTT formulated reduced QFT decay exponentially with  $n$ .

The QTTTO version of the QFT was dubbed the Superfast Fourier Transform (SFFT) [15], as it was observed that for certain applications, the SFFT outperforms the regular FFT. These cases typically require the underlying data for the SFFT to be structured

We will adopt a similar approach by restricting ourselves to the reduced form and deriving the SFFT. However, this leads to a different convention for the momentum space, which must be considered for the Green-Eshelby operator in the upcoming section. It is worth noting that even on current NISQ-era quantum hardware, the reordering operation can cause issues due to the numerous error-prone  $SWAP$  operators [32].

### 4.2 The Zip-Up Algorithm

The "Zip-Up" algorithm can be used to convert any quantum circuit into a TTO through a combination of tensor contractions and SVDs [33]. In the following, we will explain the algorithm by transferring the reduced QFT into the SFFT.

Before applying the procedure on the QFT quantum circuit, we must perform preliminary preparations by decomposing the controlled quantum gates and recombining them in a slightly more favourable manner. In this case, this means separating the controlled Phase-Gates into a 'control' and a 'phase' components. Mathematically, this is achieved by representing the full gate as a separated inner product of the following form

$$cP(\theta) = |0\rangle\langle 0| \otimes \mathbb{1} + |1\rangle\langle 1| \otimes P(\theta)$$

$$= \underbrace{(|0\rangle\langle 0| \quad |1\rangle\langle 1|)}_{\text{copy}} \underbrace{\begin{pmatrix} \mathbb{1} \\ P(\theta) \end{pmatrix}}_{\text{3-phase}}.$$

This results in a combination of a Copy Gate and a 3-legged Phase Gate (or simply 3-phase gate), as shown in Figure 3 a). We then separate all controlled Phase gates into such pairs. The resulting copy gates enforce that all legs correspond to the same state. Therefore, the copy gates can be interchanged as long as the total incoming and outgoing dimensions, or 'legs', remain fixed. Intuitively this can be described through a diagrammatic representation, see Figure 3 b).

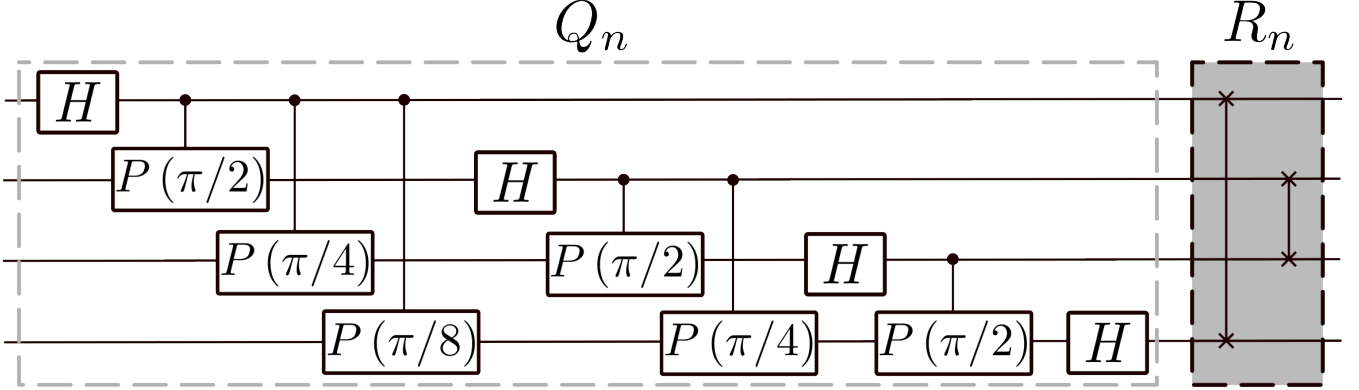


**Figure 1** Quantum Circuit for the Quantum Fourier Transform  $QFT_n = R_n Q_n$  for  $n = 4$ .

These reordered copy gates can be recombined with the 3-phase gates, as shown in Figure 3 c), resulting in a novel 4-legged phase gate (or 4-phase gate). It should be noted that although we recombine the copy and 3-phase gates, the incoming and outgoing dimensions have changed.

With our prepared mathematical construct, we can reformulate the reduced QFT into QTT format using the Zip-Up algorithm. Figure 2 a) shows the diagrammatic representation of the Zip-Up algorithm, while the specific transformations required to perform the block contractions are shown in b).

The algorithm begins by contracting the tensor on the least significant qubit with its right neighbour along their shared index. In the second step, this new tensor is reshaped into a matrix. The incoming and outgoing dimensions of the matrix are determined by specific leg combinations. Since the algorithm starts from the bottom and goes to the top, the vertical as well as the downward legs get combined into the outgoing dimension, while the upward legs form the incoming dimension. As a next step, a SVD is performed on this matrix. The  $V$ -matrix remains, while the  $U$  and  $S$  matrices get recombined. As a last sub-step, the remaining two matrices get reshaped back into tensor form, where special care needs to be taken into separating the legs into their original form.

In the next iteration of the procedure, the resulting  $V$ -tensor remains at the original position, while the  $US$ -tensor gets contracted with the two tensors acting on the next upper neighbouring qubit, see Figure 2. This procedure is repeated until the most significant qubit is reached. Now the procedure restarts by recombining the  $V$ -tensor acting on the least significant qubit with its right neighbour ( $V_4$  in Figure 2). The full down-top procedure is performed until there is only one tensor acting per qubit left.

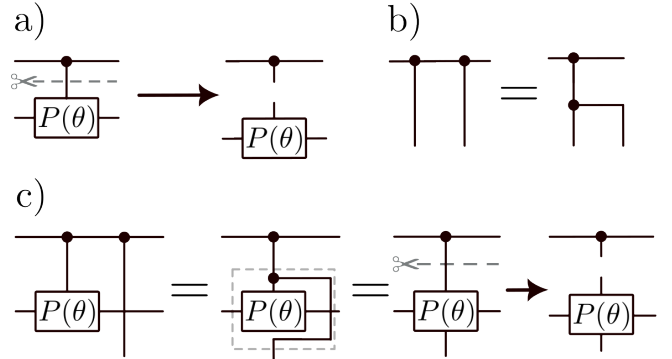


**Figure 3** Diagrammatic representation of a) separation, b) reordering and c) recombining of the controlled phase gate into copy, 3-phase and 4-phase gates [14].

### 4.3 SFFT-based Homogenization

To derive the SFFT-based Homogenization algorithm, the corresponding states and operators of the FFT-based algorithm 1 must be transferred into QTT or QTTO format. The only naturally occurring operators are the FFT and its inverse, which are simply replaced by the novel (inverse) SFFT operator, denoted as  $\mathcal{S}^{(-1)}$ . The other states - namely, the local strain  $\varepsilon(\mathbf{x})$ , the mean strain  $\mathbf{E}$ , the Green-Eshelby Operator  $\hat{T}_0(\mathbf{q})$  and the local and isotropic reference stiffness  $\mathbf{C}(\mathbf{x})$  and  $\mathbf{C}_0$  - must be formulated in QTT format. To achieve this, we begin by discretizing the  $\mathbf{x}$  or  $\mathbf{q}$  dependent states in a binary fashion. This means that, instead of discretizing a function  $t(x)$  using a single grid variable  $k$ , according to

$$t(x) \approx t[(k-1)\Delta x] = F(k),$$

the different grid points are specified by a multi-index formulation in the form of binary fractions

$$t(x) \approx t\left(\frac{b_1}{2} + \frac{b_2}{4} + \dots + \frac{b_n}{2^n}\right) = \mathcal{T}(b_1 b_2 \dots b_n). \quad (13)$$

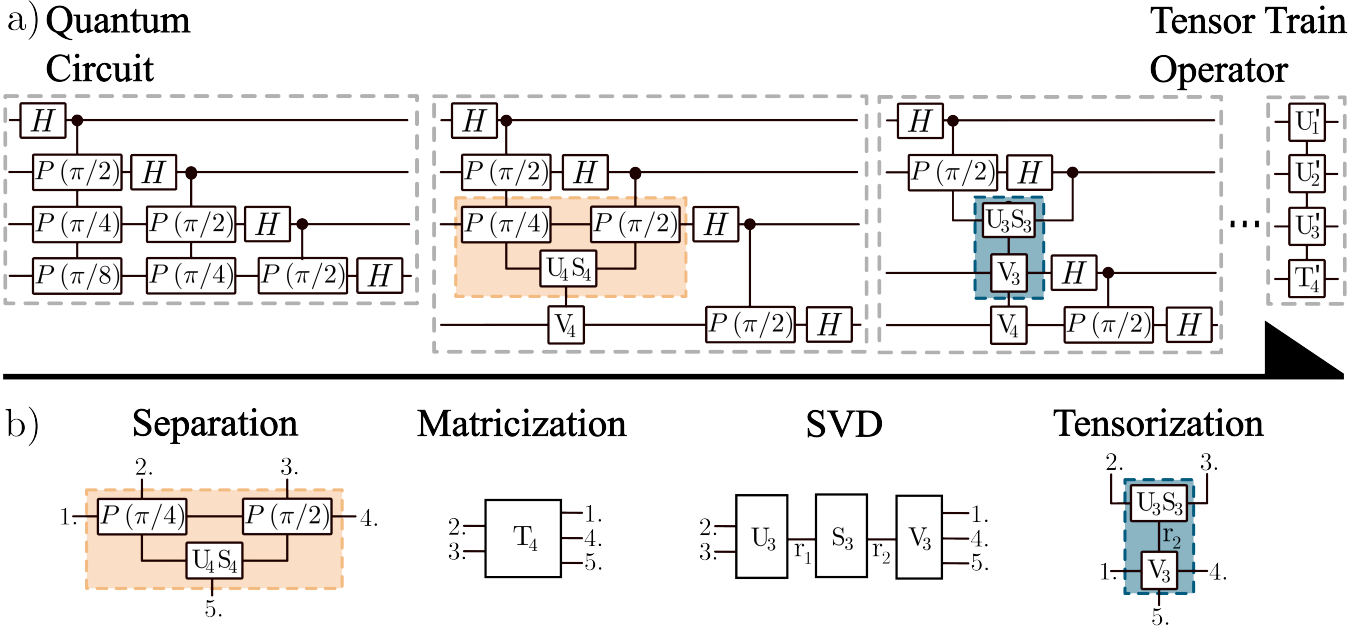


**Figure 2** a) The first few steps of Zip-Up Algorithm in example of the QFT for the full Quantum Circuit; b) The detailed transformations needed within one step of the Zip-Up algorithm.

Although the function is evaluated at the same grid points, the resulting tensor has a different number of physical indices and corresponding dimensions. The binary discretization method yields an  $n$ -order tensor with dimensionality  $d = 2$  per index, which mirrors the physical indices required for the QTT format. Once the high-order tensor is obtained, the QTT cores can be separated easily by applying the (randomized) TT-SVD or Tensor-Cross-Approximation [29, 34], as detailed in Appendix D.

In our multidimensional case, the dimensions are processed sequentially, resulting in QTT representations where the cores are grouped by dimension. We assume  $N = 2^n$  discretization points per dimension, corresponding to  $n$  QTT cores (similar to  $n$  qubits) per dimension.

Two constant operators are required for the algorithm's iterative procedure: the mean-strain  $\mathbf{E}$  and the isotropic reference stiffness  $\mathbf{C}_0$ . These special cases can easily be formulated by a QTT of rank one by directly generating the cores using  $(2 \times 2)$  identity matrices, resulting in core shapes of  $(2 \times 1 \times 2 \times 1)$ . Multiplying one of the cores with the constant value associated with the respective functions results in their respective QTT.

Until now, we have only discussed the internal structures of the tensors in the context of the required discretization. However, the tensors in question generally yield multidimensional outputs, introducing additional physical indices. Here, we are considering the original tensors in voigt notation resulting in a simplified operator structure. One approach to handle these indices is

to treat the states as vectors (or matrices), with their elements in QTT format. Although this approach is justifiable, exploiting the computational benefits of the TT optimization algorithms would not be feasible.

To obtain a full TT representation, we make a slight deviate from the QTT format by adding a single additional core at the beginning of the QTT. This core is permitted to deviate from the imposed dimensionality dictated by the QTT and serves as a control for the different components of the Voigt formulation. Thus, it holds the information about the Voigt arithmetic rather than the discretization of the function. Therefore, we refer to this version as the controlled QTT (cQTT). This approach generalizes naturally to incorporate controlled QTTOs (cQTTOs).

After obtaining cQTTs and cQTTOs representations for all states, it is computationally advantageous to raise the cQTTs - prominent in the Hadamard multiplications of the algorithm - to cQTTOs, as explained in section 3. This allows for either simple contractions or optimization methods, which are preferable to perform these costly products. This is especially important for the Green-Eshelby Operator due to its comparably high rank structure, for which the AMEn optimization algorithm  $\mathcal{A}(\cdot, \cdot)$  will be employed.

Since the Green-Eshelby operator  $\hat{T}_0$  resides in the momentum space, it must be treated differently. This is because of the required momentum-space convention of using the SFFT over the FFT. As discussed in section 4.1, a reordering of the cores is necessary. This involves

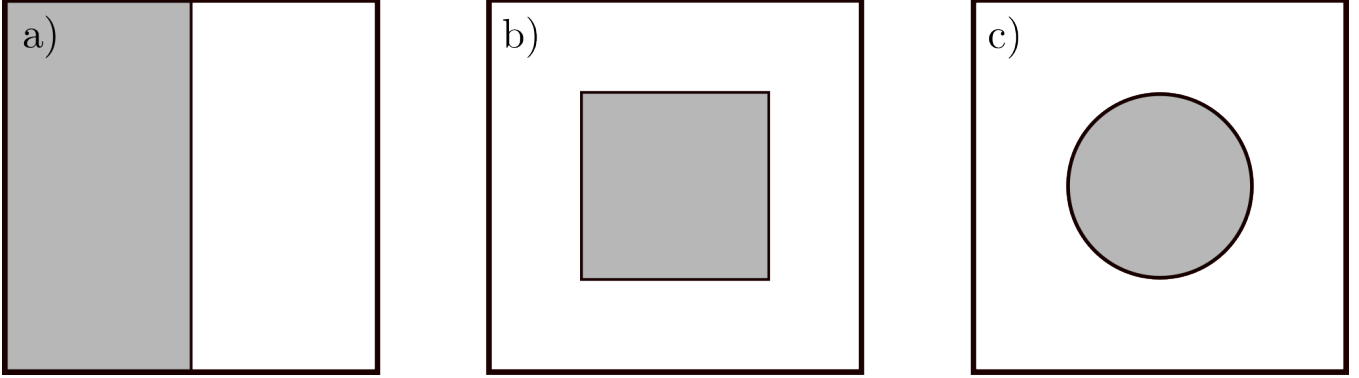


**Figure 4** Fundamental 2D geometries used to probe the regimes of the SFFT-based Homogenization algorithm: a) Laminate, b) Square and c) Circle. The grey regions have a Young’s Modulus of  $E_1 = 29/3$  GPa while the white regions display  $E_2 = 4/3$  GPa. The Poisson ratios were set to  $\nu_1 = \nu_2 = 1/3$  for the grey and white regions, respectively.

two steps: 1) The indices per geometrical dimension  $D$  of the initial discretization tensor, obtained through equation (13), must be reversed. 2) The tensor must be complex conjugated. Performing these additional steps for operators in the momentum space ensures the correct convention according to the SFFT, yielding our final form of the SFFT-based Homogenization algorithm 2.

---

**Algorithm 2:** SFFT-based Homogenization Algorithm

---

**Input:** Mean strain field  $\varepsilon_0 = \mathbf{E}$

**while** *not converged* **do**

$$\tau_m = (\mathbf{C} - \mathbf{C}_0) \varepsilon_m$$

$$\hat{\tau}_m = \mathcal{S}[\tau_m]$$

$$\hat{\varepsilon}_m = \mathcal{A}(\hat{I}_0, \hat{\tau}_m)$$

$$\varepsilon_{m+1} = \mathbf{E} - \mathcal{S}^{-1}[\hat{\varepsilon}_m]$$

$$m = m + 1$$

**if**  $\|\frac{\varepsilon_{m+1} - \varepsilon_m}{\mathbf{E}}\|_F < \delta_{\text{tol}}$  **then**  
| break;

**end**

**end**

**Return:** Local strain field  $\varepsilon_{m+1}$

---

## 5 Experiments

We evaluated the performance of the SFFT-based Homogenization algorithm across various geometries to assess its applicability in diverse scenarios. The primary geometries used in this study are shown in Figure 4. Additional tests were also conducted on various geometries in both 2D and 3D space, as detailed in Appendix E.”

### 5.1 Setup and Preprocessing

Before executing the algorithm, all states and operators were converted into the cQTT format. The correspond-

ing preprocessing time can be reduced by storing operators in lookup tables for future runs, as most of them can be reused, minimizing overhead. A more detailed exploration of preprocessing scalability and potential improvements can be found in Appendix D.

The geometries shown in Figure 4 were analysed in 2D, with two possible generalizations considered for 3D space. The first generalization extends the geometries by adding a trivial, non-varying z-component, turning the 2D Laminate into a 3D Laminate, the Square into a Pillar, and the Circle into a Spherical Pillar. The second generalization assumes that the geometries in Figure 4 are viewed identically from every direction, resulting in the Square becoming a Box and the Circle becoming a Sphere. The Laminate is limited to only a trivial generalization.

The accuracy of the SFFT method was evaluated by calculating the relative error in the stress solution field

$$\Delta\bar{\sigma} = \mathbb{E} \left[ \frac{|\sigma^{\text{SFFT}}(\mathbf{x}) - \sigma^{\text{FFT}}(\mathbf{x})|}{|\sigma^{\text{FFT}}(\mathbf{x})|} \right], \quad (14)$$

where  $\sigma^{\text{SFFT}}$  and  $\sigma^{\text{FFT}}$  are the stress fields obtained after convergence of the SFFT- and FFT-based Homogenization algorithms, respectively.

Unless otherwise specified, all experiments used a cQTT and cQTT0 accuracy parameter of  $\delta_{\text{acc}} = 10^{-6}$  and a convergence threshold of  $\delta_{\text{tol}} = 10^{-4}$ . The discretization followed a ‘staggered grid’ approach, as outlined in Appendix F. For clarity, the discretization order  $n$  is used throughout, where  $N = 2^n$  represents the number of discretization points per dimension  $D$ .

Due to memory and time constraints, not all runs were performed for each discretization order. In these cases, missing points are extrapolated and connected by dashed lines in the subsequent graphs.



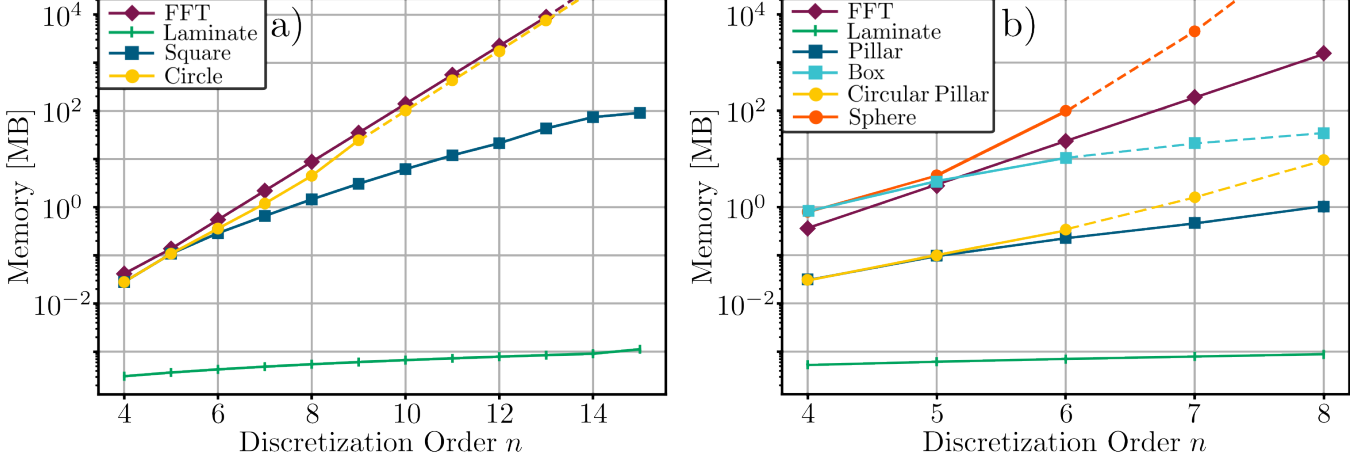


**Figure 5** Maximal Memory used for storing the local strain in dependence of the discretization order  $n$  in a) 2D and b) 3D space.

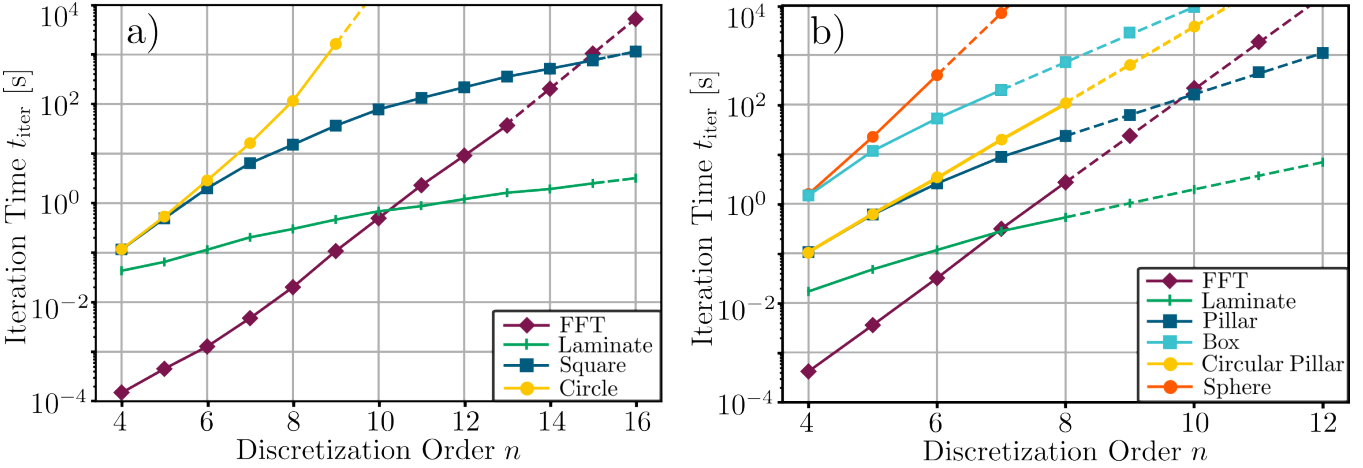


**Figure 6** Average iteration time  $t_{\text{iter}}$  in dependence of the discretization order  $n$  in a) 2D and b) 3D space.

## 5.2 Performance Comparison

In our experiments, we compared the SFFT-based algorithm 2 with the traditional FFT-based approach 1 by measuring memory consumption and iteration times across different geometries and discretization orders.

The memory consumption results shown in Figure 5 highlight the exponential scaling of the FFT-based approach, in contrast to the geometry-specific advantages of the SFFT method in both 2D and 3D. For 1D-like geometries, such as the Laminate, the SFFT method significantly reduces memory usage. The Square Pillar and Box geometries demonstrate sub-exponential scaling, reflecting the adaptability of the SFFT method. In contrast, the Circle and Circular Pillar exhibit exponential scaling similar to the FFT method, while the Sphere performs even slightly worse than the FFT method. Notably, trivially generalized structures, such as the Pillar and Circular Pillar, show improved memory efficiency over their FFT baseline when compared to their 2D

counterparts. This is a direct consequence of the additional dimension not increasing complexity for the SFFT due to its geometry-tailored approach.

The iteration times, shown in Figure 6, reveal that for smaller discretization orders  $n$ , the FFT-based method is faster. However, the SFFT outperforms the FFT beyond a geometry-dependent crossover point. In 2D, the Laminate crosses over at  $n = 11$ , followed by the Square at  $n = 15$ . In 3D, the Laminate reaches the crossover substantially quicker at  $n = 7$ , while both the Pillar and Circular Pillar geometries reach the crossover at a reasonable order of  $n = 10$ . Furthermore, the plot indicates that for even higher discretization orders, the Box will exhibit a crossover around  $n = 15$ , aligning with the 2D results. Although no crossover is expected for the Circle and Sphere, the Circular Pillar may experience one at very high discretizations, suggesting that trivially generalized 3D structures may always have a crossover point. While this discretization order would

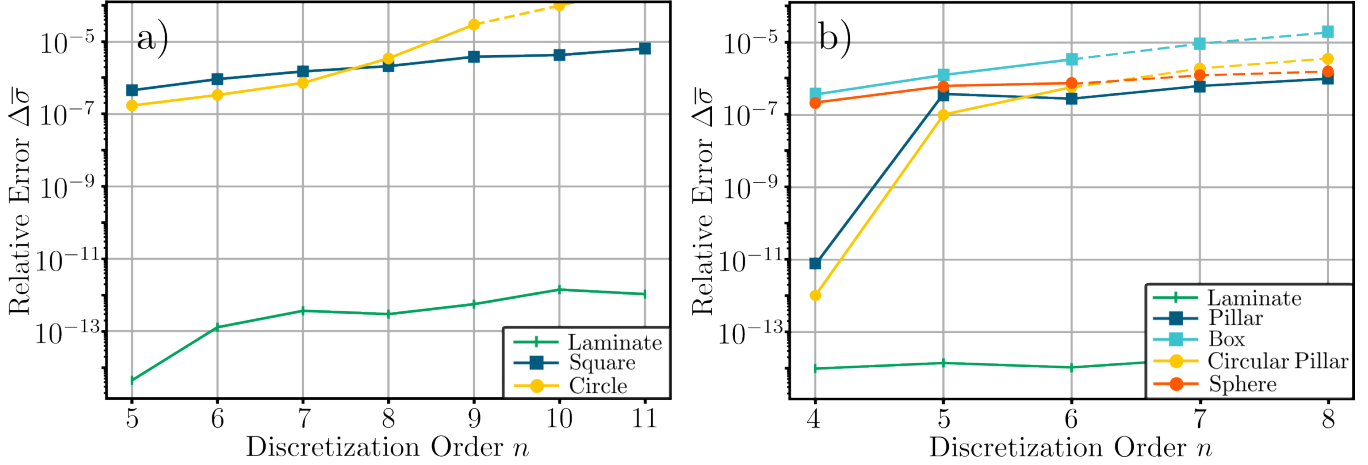


**Figure 7** Relative Error  $\Delta\bar{\sigma}$  in dependence of the discretization order  $n$  in a) 2D and b) 3D space.

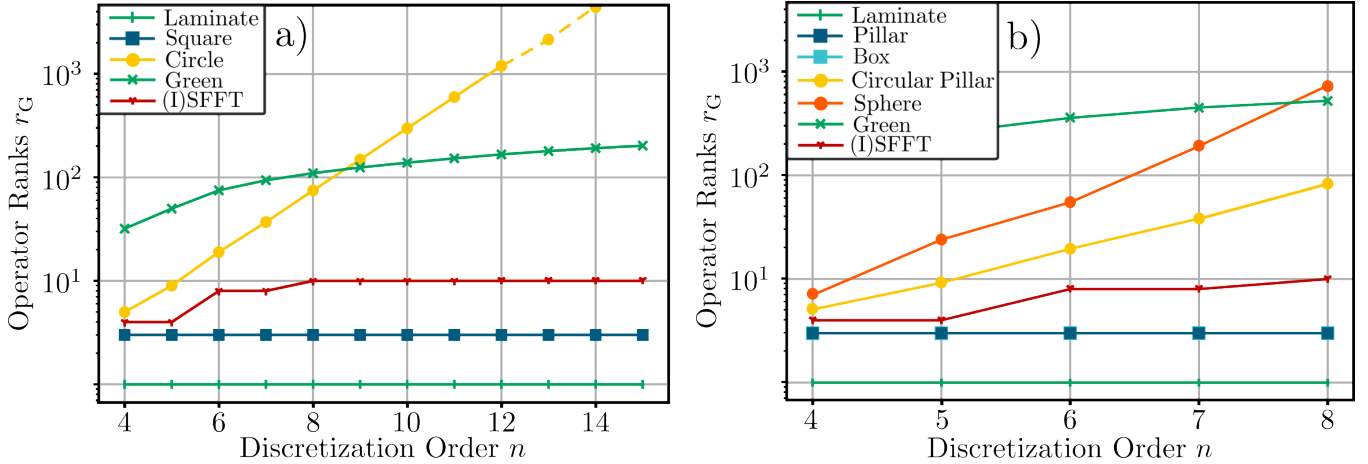


**Figure 8** Ranks obtained in dependence of the discretization order  $n$ : the Stiffness Operators  $\mathbf{C}$  for the different Geometries, the Green-Eshelby as well as the (I)SFFT Operators in a) 2D and b) 3D. The rounding accuracy was set to  $\delta_{\text{acc}} = 10^{-10}$ .

be far to high for any real-world application, this may suggest that trivially generalized 3D structures may always exhibit a crossover point due to the negligible third dimension. It should be noted that the FFT baseline benefits from highly optimized libraries, while similarly optimized code is not yet available for the SFFT-based Homogenization. Thus, we expect that further optimizations to the SFFT implementation will noticeably reduce the order at which crossover points occur.

Furthermore, it is worth noting that the iteration times between the Square and Circle and their trivial extensions, the Pillar and Circular Pillar, respectively, are almost negligible. The minor difference is primarily due to the non-negligible contribution of the Green-Eshelby Operator in 3D.

Figure 7 shows the error dependence on the discretization order  $n$ . For the Laminate, the analytic solution is achieved after just one iteration, resulting in a signifi-

cantly reduced relative error. For other geometries, the relative error stabilizes around  $10^{-5}$  for both 2D and 3D cases, well within the acceptable range for industrial applications. The error remains close to the rounding accuracy of the cQTTs of  $\delta_{\text{acc}}$ , see equation (12).

Figure 8 shows that the SFFT and ISFFT cQTT ranks converge to  $r_G = 10$  after  $n = 8$  in both 2D and 3D, indicating the efficiency and scalability of the respective operators. The Green-Eshelby operator exhibits approximately linear rank growth across discretization and dimension, further demonstrating the favourable scaling of the non-geometry-dependent parts of the SFFT approach. Therefore, the applicability of SFFT-based Homogenization is limited by the compressibility of the underlying geometry. The Circle and its 3D counterparts consistently exhibit exponential rank growth, highlighting the inherent incompatibility of these geometries with the SFFT approach. This is further supported by Fig-

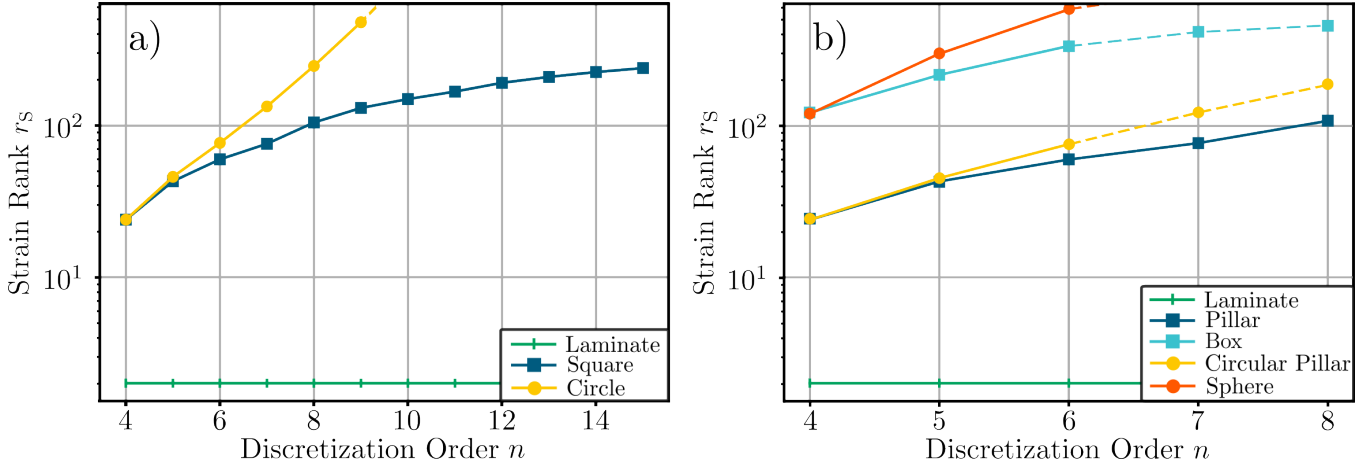


**Figure 9** Maximal Strain Rank  $r_s$  during the evaluation of the algorithm in dependence of the discretization order  $n$  in a) 2D and b) 3D space.

ure 9, where similar growth patterns are observed for the strain rank  $r_s$  of the respective geometries.

These results suggest that it may be possible to quickly estimate the applicability of the SFFT-based Homogenization by compressing the geometries at two different discretization orders. This approach could provide an initial indication of both the rank and its growth behaviour, helping to assess whether a geometry is suitable for our approach.

Finally, it is worth noting that in the FFT-based Homogenization, iteration times are primarily limited by the FFT computation itself. In contrast, our SFFT-based approach shifts the computational bottleneck to the matrix-vector product between the Green-Eshelby cQTT and the strain cQTT. This operation typically accounts for more than 95% of the total computation time due to the relatively high ranks of both the Green-Eshelby operator and the strain during the iterative procedure. This distinction underscores a key area for potential optimization in our method. Since the full scalability limits of the SFFT have not yet been reached, improving the efficiency of this matrix-vector product could lead to substantial performance gains.

### 5.3 Solution Fields

The stress solution fields obtained using the SFFT-based Homogenization algorithm were compared to the FFT-based approach for both the Box and Circle geometries, see Figure 10). For both geometries, the relative error in the solution fields is greatest at the boundaries of the inclusion. Interestingly, for the Circle geometry, rectangular regions with similar relative error are observed. This suggests that the cQTT format is better suited for handling straight, non-curved edges in the ge-

ometry. To accommodate curved geometries within the SFFT-based Homogenization framework, alternative TN architectures, such as PEPS, MERA, or other generalizations of TTNs, may prove beneficial. However, this analysis lies outside the scope of the current paper and will be addressed in future work.

## 6 Conclusion

In this paper, we introduce the SFFT-based Homogenization, a geometry-tailored adaptation of the FFT-based Homogenization method that leverages the cQTT variant of the QFT, known as the SFFT. This novel algorithm offers key advantages, including improved time complexity and reduced memory consumption, outperforming the traditional FFT-based approach in scenarios where the geometry can be effectively compressed into a low-rank cQTT format. The advantage stems from the tailored nature of our method in contrast to the 'one-size-fits-all' approach of the FFT-based method. Notably, memory consumption no longer scales exponentially and consistently outperforms the FFT-based approach in relevant cases.

While the FFT-based approach retains an advantage for smaller discretizations, the SFFT-based algorithm surpasses it beyond a geometry-dependent crossover. Beyond this point, the improved time complexity of our method leads to a substantial speedup. These benefits are particularly pronounced in 3D settings with compressible 2D or 1D structures, where the additional dimensions represent redundant data that the SFFT can efficiently handle.

However, the current version of our algorithm struggles with geometries featuring circular inclusions, possibly due to the specific choice of the underlying TN archi-

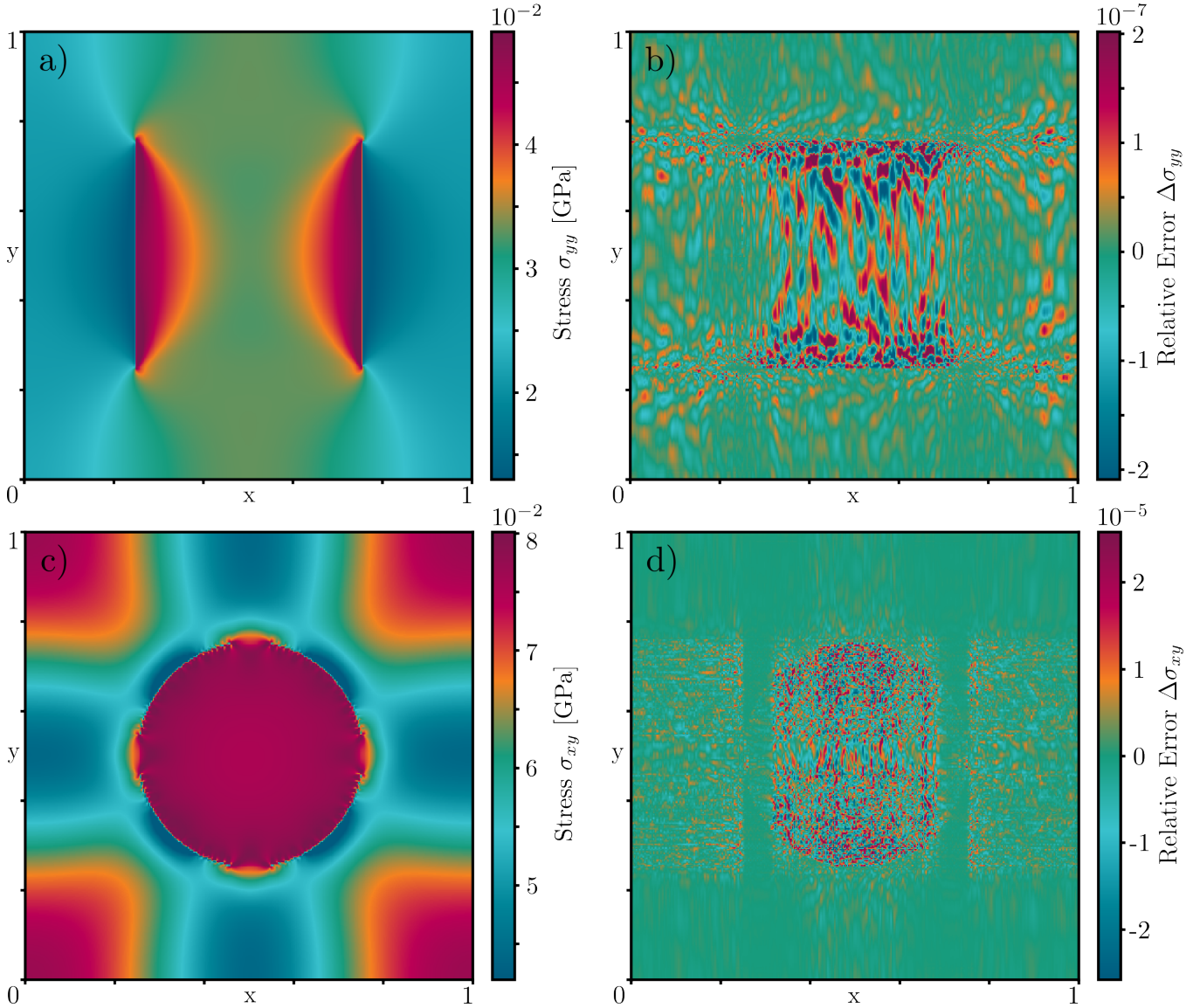


**Figure 10** a) Stress field  $\sigma_{yy}$  under tensile load and b)  $\sigma_{xy}$  under shear load; c) relative error  $\Delta\sigma_{yy}$  for the Square geometry and d)  $\Delta\sigma_{xy}$  for the Circle geometry, evaluated with  $n = 8$  using the cQTT- and FFT-based approaches.

ture. This raises the question of whether alternative network architectures, such as PEPS or TTN, could address this shortcoming.

Leveraging GPUs for high discretizations, made possible by reduced memory consumption, presents another potential enhancement [35]. This capability is infeasible for traditional FFT-based Homogenization at high discretizations. Similarly, utilizing TPUs [36] and optimizing the underlying software could provide substantial speedups, potentially offering a decisive advantage to the SFFT-based Homogenization algorithm. This is further supported by the observation that the anticipated bottleneck imposed by the SFFT has not yet been reached, with runtime instead dominated by the multiplication of the Green-Eshelby operator and the intermediate strain.

## Acknowledgments

We thank BMWK for the financial support provided under the EniQmA project. Furthermore, we acknowledge the funding of the German National High Performance Computing (NHR) Association for the Center NHR South-West.

- 1 C. C. Mei, J.-L. Auriault, and C.-O. Ng. Some applications of the homogenization theory. *Adv. Appl. Mech.*, 32:277–348, 1996.
- 2 P. D. Jablonski and J. A. Hawk. Homogenizing advanced alloys: Thermodynamic and kinetic simulations followed by experimental results. *JMEPEG*, 26:4–13, 2016.
- 3 Y. Wang, L. Hou, H. Su, Q. Tian K. Yu, D. Eskin, L. Katgerman, and L. Zhuang. Tuning homogenization of high-

- strength aluminum alloys through thermodynamic alloying approach. *Mater. Des.*, 221:110975, 2022.
- 4 N. Bakhvalov and G. Panasenko. *Homogenisation: Averaging Processes in Periodic Media*. Kluwer Academic Publishers, 1989.
  - 5 H. Moulinec and P. Suquet. A numerical method for computing the overall response of nonlinear composites with complex microstructure. *Comput. Methods Appl. Mech. Eng.*, 157:69–94, 1998.
  - 6 C. Toulemonde, R. Masson, and J. El Gharib. Modeling the effective elastic behavior of composites: a mixed finite element and homogenisation approach. *Comptes Rendus Mécanique*, 336:275–282, 2008.
  - 7 M. Leuschner and F. Fritzen. Fourier-accelerated nodal solvers (fans) for homogenization problems. *Comput. Mech.*, 62:359–392, 2018.
  - 8 M. Schneider, D. Merkert, and M. Kabel. Fft-based homogenization for microstructures discretized by linear hexahedral elements. *Int. J. Numer. Methods Eng.*, 109:1461–1489, 2017.
  - 9 M. Schneider. A review of nonlinear fft-based computational homogenization methods. *Acta Mechanica*, 232:2051–2100, 2021.
  - 10 B. Liu, M. Ortiz, and F. Cirak. Towards quantum computational mechanics. *Comput. Methods Appl. Mech. Eng.*, 432:117403, 2024.
  - 11 F. Givois, M. Kabel, and N. Gauger. Qft-based homogenization. 2022.
  - 12 J. Vondrejč, D. Liu, M. Ladecky, and H. G. Matthies. Fft-based homogenisation accelerated by low-rank tensor approximations. *Comput. Methods Appl. Mech. Eng.*, 364:112890, 2020.
  - 13 L. Risthaus and M. Schneider. Imposing different boundary conditions for thermal computational homogenization problems with fft- and tensor-train-based green’s operator methods. *Int J Numer Methods Eng.*, 125, 2024.
  - 14 J. Chen, E. M. Stoudenmire, and S. R. White. Quantum fourier transform has small entanglement. *PRX Quantum*, 4:040318, 2023.
  - 15 S. Dolgov, B. Khoromskij, and D. Savostyanov. Superfast fourier transform using qtt approximation. *J. Fourier Anal. Appl.*, 18:915–953, 2012.
  - 16 D. Cioranescu and P. Donato. *An Introduction to Homogenization*. Oxford University Press, 1999.
  - 17 S. Brisard and L. Dormieux. Fft-based methods for the mechanics of composites: a general variational framework. *Comp. Mat. Science*, 49:663–671, 2010.
  - 18 H. Grimm-Strele and M. Kabel. Fft-based homogenization with mixed uniform boundary conditions. *Int. J. Numer. Methods Eng.*, 122:7241–7265, 2021.
  - 19 F. Willot. Fourier-based schemes for computing the mechanical response of composites with accurate local fields. *C. R. Mécanique*, 343:232–245, 2015.
  - 20 D. Schwarzenbach. *Kristallographie*. Springer, 2013.
  - 21 E. Kornev, S. Dolgov, K. Pinto, M. Pflictsch, M. Perelshtein, and A. Melnikov. Numerical solution of the incompressible navier-stokes equations for chemical mixers via quantum inspired tensor train finite element method. 2023.
  - 22 W. Hackbusch and S. Kühn. A new scheme for the tensor representation. *JFFA*, 15:706–722, 2009.
  - 23 M. Fannes, B. Nachtergaele, and R. F. Werner. Finitely correlated states on quantum spin chains. *Commun. Math. Phys.*, 144:443–490, 1992.
  - 24 Y.-Y. Shi, L.-M. Duan, and G. Vidal. Classical simulation of quantum many-body systems with a tree tensor network. *Phys. Rev. A*, 74, 2006.
  - 25 R. Orús. A practical introduction to tensor networks: Matrix product states and projected entangled pair states. *Annals of Physics*, 349:117–158, 2014.
  - 26 S. Montangero. *Introduction to Tensor Network Methods*. Springer, 2018.
  - 27 J. Biamonte and V. Bergholm. Quantum tensor networks in a nutshell. 2023.
  - 28 G Evenbly and G Vidal. Tensor network states and geometry. *J. Stat. Phys.*, 145:891, 2011.
  - 29 I. V. Oseledets. Tensor-train ranks for matrices and their inverses. *SIAM J. Sci. Comput.*, 33:2295–2317, 2011.
  - 30 S. V. Dolgov and D. V. Savostyanov. Alternating minimal energy methods for linear systems in higher dimensions. part ii: Faster algorithm and application to nonsymmetric systems. *SIAM J. Sci. Comput.*, 36:A2248–A2271, 2014.
  - 31 J. J. García-Ripoll. Quantum-inspired algorithms for multivariate analysis: from interpolation to partial differential equations. *Quantum*, 5:431, 2021.
  - 32 K. C. Nowack, M. Shafiei, M. Laforest, G. E. D. K. Prawiroatmodjo, L. R. Schreiber, C. Reichl, W. Wegscheider, and L. M. K. Vandersypen. Single-shot correlations and two-qubit gate of solid-state spins. *Science*, 333:1269–1272, 2011.
  - 33 E. M. Stoudenmire and S. R. White. Minimally entangled typical thermal state algorithms. *New J. Phys.*, 12:055026, 2010.
  - 34 I. Oseledets and E. Tyrtysnikov. Tt-cross approximation for multidimensional arrays. *Linear Algebra Its Appl.*, 432:70–88, 2010.
  - 35 F. Pan, H. Gu, L. Kuang, B. Liu, and P. Zhang. Efficient quantum circuit simulation by tensor network methods on modern gpus. *ACM TQC*, 5:1–26, 2024.
  - 36 M. Ganahl, J. Beall, M. Hauru, A. G.M. Lewis, T. Wojno, J. H. Yoo, Y. Zou, and G. Vidal. Density matrix renormalization group with tensor processing units. *PRX QUANTUM*, 4:010317, 2023.
  - 37 S. Holtz, T. Rohwedder, and R. Schneider. The alternating linear scheme for tensor optimization in the tensor train format. *SIAM J. Sci. Comput.*, 34:A683, 2012.
  - 38 S. R. White. Density-matrix algorithms for quantum renormalization groups. *Phys. Rev. B*, 48:10345, 1993.
  - 39 D. Kressner, B. Vandereycken, and R. Voorhaar. Streaming tensor train approximation. *SIAM J. Sci. Comput.*, 45:A2610–A2631, 2023.
  - 40 H. Karau and M. Kimmins. *Scaling Python with Dask*. O’Reilly Media, 2023.
  - 41 N. Halko, P. G. Martinsson, and J. A. Tropp. Finding structure with randomness: Probabilistic algorithms for constructing approximate matrix decompositions. *SIAM Review*, 53:217–288, 2011.
  - 42 Y. Sato, Y. L. Terashima, and R. Kondo. Efficient computational homogenization via tensor train format. 2024.

| Scheme Name | Divergence Operator $k_j(\mathbf{q})$  |
|-------------|--|
| Direct      | $k_j^D(\mathbf{q}) = iq_j$   |
| Centered    | $k_j^C(\mathbf{q}) = i \sin(q_j)$  |
| Forward     | $k_j^F(\mathbf{q}) = + (e^{+iq_j} - 1)$  |
| Backward    | $k_j^F(\mathbf{q}) = - (e^{-iq_j} - 1)$  |
| Hex8R       | $k_j^H(\mathbf{q}) = \frac{i}{2} \tan\left(\frac{q_j}{2}\right) \sum_l (1 + e^{iq_l})$ |
| Staggered   | $k_j^\pm(\mathbf{q}) = \pm (e^{\pm iq_j} - 1)$   |

**Table 4** Divergence Operator in momentum space for different discretization schemes [18, 19].

## Appendix A Greens operator Discretization Schemes

The discretization of computational domains and associated variables is a critical step in numerical modelling, particularly in Fourier-based methods. This appendix provides a detailed discussion of the Fourier-space discretization schemes relevant to FFT- and SFFT-based Homogenization. These schemes play a central role in ensuring accurate and efficient computations, particularly by addressing numerical artifacts and ensuring physical consistency in derived quantities.

The specific form of the Green-Eshelby operator determines the choice of the discretization scheme used. This dependency arises directly from the mathematical formulation of the divergence operator in Fourier space, which specifies how variables such as strain and stress are represented and manipulated, according to

$$k_i(\mathbf{q}) \sigma_{ij}(\mathbf{q}) = 0$$

$$\varepsilon_{ij} = (\mathbf{q}) \frac{1}{2} [k_i(\mathbf{q}) u_j(\mathbf{q}) + k_j(\mathbf{q}) u_i(\mathbf{q})].$$

To begin, the domain  $V \equiv L^D$  (here  $L = 1$ ) is discretized into  $N^D$  pixel/voxels, resulting in the Fourier modes

$$q_i = \frac{2\pi}{NL} \xi_i$$

with fundamental frequencies

$$\xi_i = \begin{cases} (-\frac{N}{2} + 1), (-\frac{N}{2} + 2), \dots, -1, 0, +1, \dots, (\frac{N}{2} - 1), \frac{N}{2} & \text{even } N, \\ (-\frac{N-1}{2}), (-\frac{N-3}{2}), \dots, -1, 0, +1, \dots, (\frac{N-3}{2}), (\frac{N-1}{2}) & \text{odd } N. \end{cases}$$

These Fourier modes are used to define an explicit representation of the Green-Eshelby operator in momentum space as

$$\hat{\Gamma}_{ij,kl}^0(\mathbf{q}) = \left[ q_i (q_m \mathbf{C}_{m,j,kn}^0 q_n)^{-1} q_l \right]_{\text{sym}}, \quad (\text{a1})$$

where the subscript 'sym' indicates the minor symmetry of the index pairs  $(i, j)$  and  $(k, l)$ , respectively [19].

In continuous space, the Green-Eshelby operator exhibits the symmetry  $\hat{\Gamma}^0(\mathbf{q})^* = \hat{\Gamma}^0(-\mathbf{q})$ , which ensures that the physically observable strain  $\varepsilon$  is real-valued. For an odd number of discretization points, this symmetry is inherently preserved in the discretized version of the operator. However, for an even number of discretization points, the Nyquist frequency becomes part of the spectrum but lacks a negative counterpart. This may result in symmetry breaking, which in this context is a purely numerical artifact that must be addressed accordingly. The approach we follow enforces symmetry at the Nyquist frequencies  $q_{ny}$  explicitly through

$$\Gamma^0(\mathbf{q}_{ny}) \rightarrow \frac{\Gamma^0(\mathbf{q}_{ny})^* + \Gamma^0(-\mathbf{q}_{ny})}{2}.$$

By combining the Green-Eshelby operators derived from the different discretization schemes listed in Table 4 -excluding the staggered grid scheme -with equation (a1), we obtain the compact form

$$\hat{\Gamma}_{ij,lm}^0, \text{gen}(\mathbf{k}) = \frac{(\lambda^0 + 2\mu^0) \left( k_i k_j \delta_{jl} \right)_{\text{sym}} + \lambda^0 \left( k_i k_m^* s_{ijl} \right)_{\text{sym}}}{\mu^0 [2(\lambda^0 + \mu^0) - \lambda^0 |\mathbf{k}^2|^2]} - \frac{\left[ \frac{\lambda^0}{\mu^0} \Re(k_i k_j^*) \Re(k_l k_m^*) + k_i k_j k_l^* k_m^* \right]}{|\mathbf{k}^2| [2(\lambda^0 + \mu^0) - \lambda^0 |\mathbf{k}^2|^2]}.$$

where  $\lambda^0$  and  $\mu^0$  are the lamé parameters of the underlying geometry [19]. Additionally, the symmetry operator  $s_{ijk}$  was introduced

$$s_{ijl} = \begin{cases} +\frac{4}{|\mathbf{k}|^4} \Im(k_i k_k^*)^2 & i \neq j = l, \\ -\frac{4}{|\mathbf{k}|^4} \Im(k_l k_j^*) \Im(k_l k_i^*) & i \neq j \neq l \neq i, \\ 0 & \text{else.} \end{cases}$$

The staggered grid discretization scheme differs from the generic schemes due to its dual formulation, which simultaneously employs both backward and forward discretization schemes. For this case, the Green-Eshelby operator [18], see equation (a1), can be reformulated as

$$\hat{I}_{ij,lm}^{0,\text{st}}(\mathbf{k}^\pm) = -\frac{1}{4\mu^0 |\mathbf{k}^\pm|^4} \left\{ [\mathbf{k}_j^- + \delta_{ij}(\mathbf{k}_j^+ - \mathbf{k}_j^-)] [\mathbf{k}_m^+ + \delta_{lm}(\mathbf{k}_m^- - \mathbf{k}_m^+)] \left( \delta_{il} + \frac{\lambda^0 + \mu^0}{\lambda^0 + 2\mu^0} \mathbf{k}_i^- \mathbf{k}_l^+ \right) \right\}_{\text{sym}}.$$

## Appendix B Approximate Tensor Train Arithmetic

A significant class of TT-TTO operations consist of optimization algorithms to solve systems of linear equations or to obtain an approximate solution to a matrix-vector product. There are many different approaches that were developed to solve these problems. The most famous ones are the alternating least square (ALS) method [37], the density matrix renormalization group (DMRG) algorithm [38] and the alternating minimal energy (AMEn) algorithm [30]. The latter one being regarded as the current state-of-the-art method.

However, instead of using the AMEn algorithm to solve liner systems of equations, we will use an adapted method for faster matrix-vector products.

We are interested in finding an approximate solution  $u$  to the equation  $Au = \tilde{v}$ , with the exact TTs  $u$  and  $\tilde{v}$ . Thus, our goal is to minimise the following cost function

$$\begin{aligned} L(\tilde{y}) &= \|v - \tilde{v}\|^2 \\ &= (v, v) - 2\Re(Au, v) + \text{const.} \end{aligned}$$

This high-dimensional optimisation problem can be reduced to a local-optimisation over the different

$$L(\tilde{y}) = (y_k, y_k) - 2\Re(\mathcal{Y}_{\neq k}^* A \mathcal{X}_{\neq k}^* x_k, y_k) + \text{const.}$$

In the above equation we used the projection operators defined through

$$y = \mathcal{Y}_{\neq k}^* y^{(k)}, \quad x = \mathcal{X}_{\neq k}^* x^{(k)},$$

where  $y_k$  and  $x_k$  are the  $k$ -th core of  $y$  and  $x$ , respectively [30].

It can readily be verified that the gradient of the cost function is zero when the following corresponding Galerkin condition is met

$$(\mathcal{Y}_{\neq k}^* A \mathcal{X}_{\neq k}^*) x_k = y_k. \tag{b2}$$

First, an initial guess for the solution is provided. The second step involves updating the first core of  $y$ , denoted as  $y_1$ , by minimizing the cost function locally. This corresponds to solving the Galerkin condition given in equation (b2).

In the third step, the residual  $z = \tilde{y} - Ax$  is computed. This step is generally computationally expensive and thus undesirable; therefore, an approximate residual  $\tilde{z} \approx z$  is used instead. Once the approximate residual is obtained, its first core is used to enrich the original first core of the solution  $y_1$ . This step, known as the Galerkin correction, not only allows for incremental refinement but, more importantly, enables an adaptive rank procedure.

It is important to note that this step is not exclusive to the AMEn algorithm; similar approaches can be found in other solvers as well.

Finally, the first core undergoes orthogonalization via QR-decomposition.

This procedure is recursively applied to all cores, and thus to all local optimization problems.

The main advantage of this class of optimization methods, compared to an exact solution, lies not only in its improved time complexity but also in the resulting rank. If the result  $y$  has a rank similar to the input TT  $x$ , the time complexity improves by a factor of  $r(A)^2$ . Moreover, the rounding procedure becomes noticeably faster, as it depends on the cubic rank. With a quasi-exact solution, the final rank scales with the product of the matrix and vector ranks.

We conclude this section by noting that we have used a revised version of the TTO-TT matrix-vector product from the TT-Toolbox available on GitHub.

## Appendix C Connection between a raised Tensor Train and its Hadamard Product

Lets assume we have two TTs  $a$  and  $b$ , defined as follows

$$\begin{aligned} a(i_1, i_2, \dots, i_n) &= a(i_1)a(i_2)\dots a(i_n), \\ b(i_1, i_2, \dots, i_n) &= b(i_1)b(i_2)\dots b(i_n). \end{aligned}$$

The next step is to raise the TT  $a$  to a TTO  $A$ , by defining the TTO cores as

$$A(i_k, j_k) = a(i_k)\delta(i_k, j_k). \tag{c3}$$

where  $\delta(\cdot, \cdot)$  is the Kronecker delta function. This operation effectively "raises" the TT into a higher-dimensional operator form. Thus, the TTO  $A$  can be written as

$$\begin{aligned} A(\{i_1, j_1\}, \{i_2, j_2\}, \dots, \{i_n, j_n\}) &= A(i_1, j_1)A(i_2, j_2)\dots A(i_n, j_n) \\ &= a(i_1)\delta(i_1, j_1)a(i_2)\delta(i_2, j_2)\dots a(i_n)\delta(i_n, j_n). \end{aligned}$$

Next, we will show that the contraction of the TTO  $A$  with another TT  $b$  results in a new TT  $c$ , which is the Hadamard product of the two TTs  $a$  and  $b$ . The contraction of  $A$  and  $b$  involves summing over the intermediate indices  $j_k$

$$\begin{aligned} c(i_1, i_2, \dots, i_n) &= \sum_{j_k} A(\{i_1, j_1\}, \{i_2, j_2\}, \dots, \{i_n, j_n\})b(j_1, j_2, \dots, j_n) \\ &= \sum_{j_k} A(i_1, j_1)A(i_2, j_2)\dots A(i_n, j_n)b(j_1)b(j_2)\dots b(j_n) \\ &= \sum_{j_k} a(i_1, j_1)a(i_2, j_2)\dots a(i_n, j_n)b(j_1)b(j_2)\dots b(j_n) \\ &= \sum_{j_k} a(i_1)\delta(i_1, j_1)a(i_2)\delta(i_2, j_2)\dots a(i_n)\delta(i_n, j_n)b(j_1)b(j_2)\dots b(j_n) \\ &= [a(i_1)a(i_2)\dots a(i_n)] [b(i_1)b(i_2)\dots b(i_n)] \\ &= a(i_1, i_2, \dots, i_n)b(i_1, i_2, \dots, i_n), \end{aligned}$$

where we used the identity from equation (c3) in the fourth line to simplify the expression. The Kronecker delta functions ensure that the contraction of the TTO with the TT results in a component-wise product between the two tensors.

Thus, raising a TT  $a$  to a TTO and contracting it with another TT  $b$  is equivalent to performing the Hadamard product between the two original TTs  $a$  and  $b$ . This shows that the contraction procedure preserves the structure of the TT and transforms the operation into a simple element-wise multiplication, which is computationally efficient, enables the usage of optimization methods and is easy to handle in practice.



## Appendix D Scalable Implementation

The implementation of the SFFT algorithm needed to achieve a certain scalability threshold for high-resolution scenarios. In this case, characterized by a large number of discretization points per dimension, we observed significant memory and time consumption during the SFFT-based algorithm’s preparation phase. This issue arises due to the reliance on the state-of-the-art TT-SVD algorithm, which is constrained by the computational bottleneck of the SVD.

As such, the SVD step scales with a complexity of  $\mathcal{O}(mn^2)$  for an  $m \times n$  matrix, where  $n < m$ . Since higher-resolution matrices scale exponentially in size, this results in exponential time consumption for separating the cores in the TT or TTO representations. Such behaviour is highly undesirable, as it merely shifts the computational burden from the iterative phase of the algorithm to the preprocessing phase.

Thus, instead of using the TT-SVD method, we will use a combination of the streamable tensor-train approximation (STTA) [39] and an updated TT-SVD method build on the randomized SVD. The specific choice of the above methods depends on the computational and memory restrictions of the compute system used.

The STTA approach can be used in a multi-core setting using pythons `dask` library [40] and is especially useful for matrices with a lower and intermediate resolution. In the high-resolution regime, we are typically encountering to high memory restrictions for the multi-core system to be beneficial. This is either due to the system not having enough memory per core or due to the high overhead of transferring the compute-graph between the nodes. In this case, the slower non-multicore version of the randomized TT-SVD with additional rank truncation threshold can be used. While the SVD of a rank  $k$  matrix with shape  $m \times n$  has a time-complexity  $\mathcal{O}(mn * \min(m, n))$  that scales quadratic, the randomized SVD only scales linear in the matrix dimensions according to  $\mathcal{O}(mn * \log(k) + (m + n) * k^2)$  [41]. Thus, we are able to speed up the process by at least a quadratic factor, which represents a significant improvement for large matrices. Alternatively, the TT-cross approximation can be used. The TT-cross method relies on a cross-approximation strategy, where the most important components of the tensor are iteratively selected to provide the best rank-reduction approximation. TT-cross selects a small subset of the tensor’s entries for its approximation, which efficiently captures the tensors structure [34]. However, since (randomized) TT-SVD is more accurate, we opted not to use TT-cross for obtaining the optimal solutions for our derived TT.

Additionally, we need to consider the case of reusing preprocessed computations for subsequent runs.

Almost all TTs and TTOs within the SFFT-based homogenization algorithm depend only on the dimensionality, the chosen resolution, and the core ordering. This includes both the (inverse) SFFT and the initial strain TT. As a result, these components can be saved in a lookup table for later use across multiple problems that share a common set of system parameters. A special case in this context is the geometry-dependent stiffness operator  $C(x, y)$  as well the Green-Eshelby operator  $\hat{\Gamma}_0(k_x, k_y)$ . The latter depends on the chosen Lamé parameters as well as the discretization scheme used. Since the Green-Eshelby operator inherently defines the discretization choice for the problem, recomputation is generally unavoidable for different schemes. However, this is not necessary for varying sets of Lamé parameters  $\{\mu, \lambda\}$ . In such cases, we can reuse the Green-Eshelby operator, which can generally be expressed in the following form

$$\hat{\Gamma}_0(k_x, k_y) = \sum_i \alpha_i(\mu, \lambda) \hat{\Gamma}^{(i)}(k_x, k_y). \tag{d4}$$

Therefore, the reduced Gamma functions  $\hat{\Gamma}^{(i)}(k_x, k_y)$  can be stored separately in TT format for efficient reuse. When needed, the prefactors  $\alpha_i(\mu, \lambda)$  can easily be computed and the saved reduced Gamma functions can be recombined according to equation (d4) into the full form through simple TT arithmetic can be easily computed, and the stored reduced Gamma functions can be recombined according to equation (d4) into the full form using simple TT arithmetic.

Finally, in contrast to all other quantities in the SFFT-based Homogenization algorithm, the stiffness operator  $C(x, y)$  must be recomputed each time a new geometry is used.

## Appendix E Additional Geometries

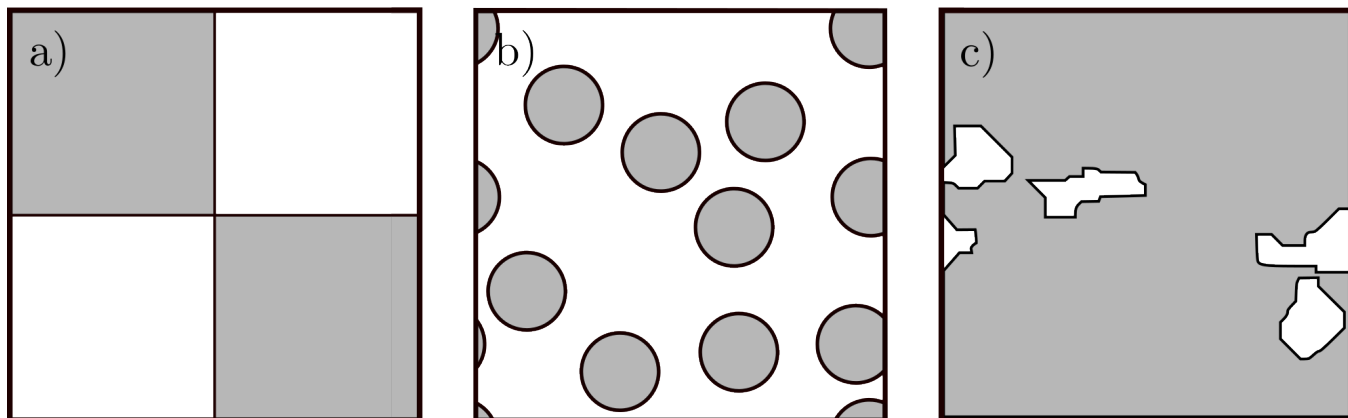


**Figure 11** Fundamental 2D geometries used to probe the regimes of the SFFT-based Homogenization algorithm: a) Checkerboard, b) Spots and c) Voronoi. The grey regions have a Young’s Modulus of  $E_1 = 29/3$  GPa while the white regions display  $E_2 = 4/3$  GPa. The Poisson ratios were set to  $\nu_1 = \nu_2 = 1/3$  for the grey and white regions, respectively.

We conducted a performance comparison between the SFFT-based algorithm and the traditional FFT-based method, evaluating memory usage and iteration times across various geometries and discretization orders.

The geometries in Figure 11 were examined in 2D, with two possible generalizations extended to 3D space. The first generalization adds a simple, non-varying z-component, transforming the Spots geometry into Fibres and the Checkerboard into the reduced Checkerboard. The second generalization assumes that the geometries in Figure 11 are viewed identically from all directions, resulting in the Checkerboard geometry becoming Checkerboard 3D and the Voronoi geometry becoming Voronoi 3D.

The Spots and Voronoi geometries were generated by sampling a fixed number of points from a uniform distribution over the RVE, which serve as the centers for the inclusions. If any Spots or Voronoi regions overlap, a new set of points is sampled. To ensure consistency across experiments, the random number generator’s seed was fixed

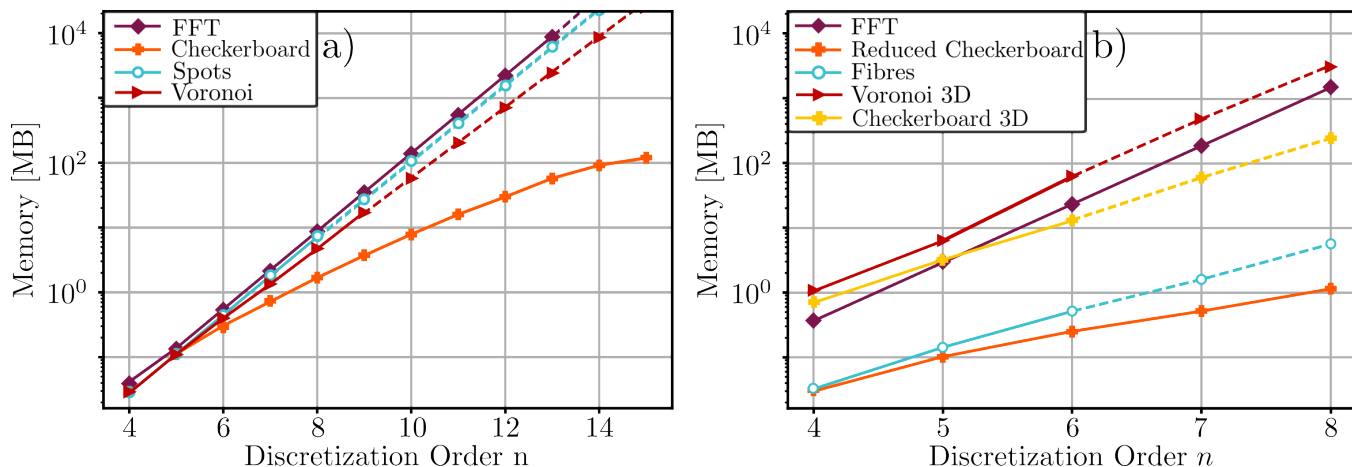


**Figure 12** Maximal Memory used for storing the local strain in dependence of the discretization order  $n$  in a) 2D and b) 3D space.

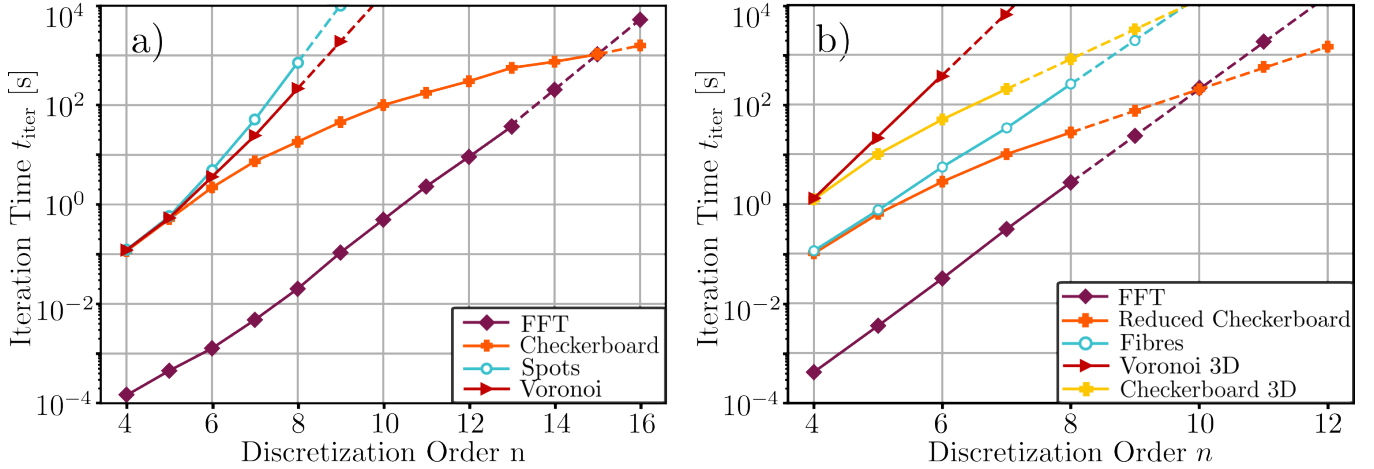


**Figure 13** Average iteration time  $t_{iter}$  in dependence of the discretization order  $n$  in a) 2D and b) 3D space.

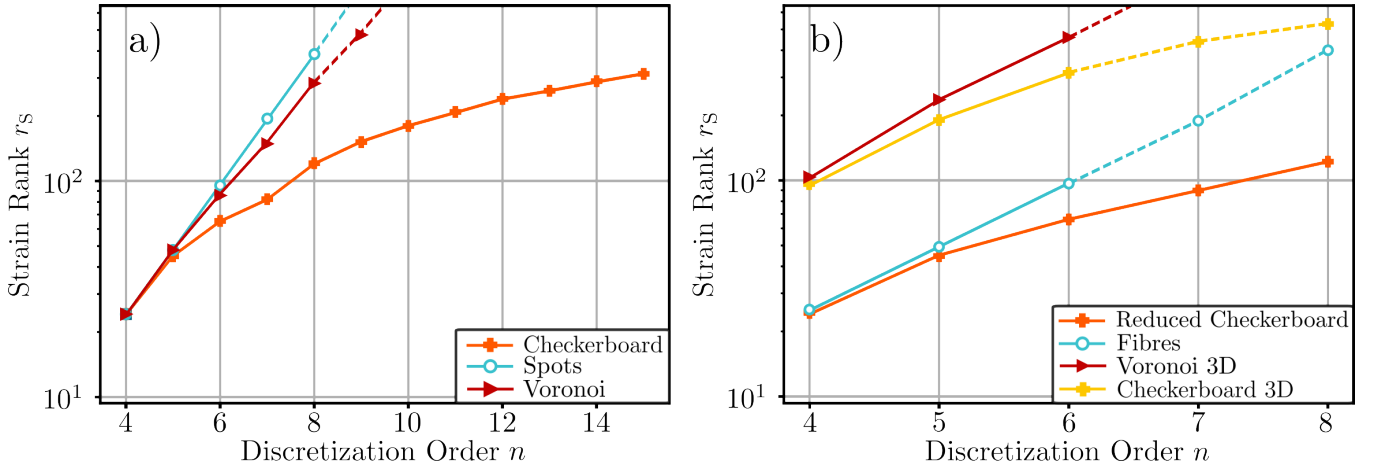


**Figure 14** Maximal Strain Rank  $r_s$  during the evaluation of the algorithm in dependence of the discretization order  $n$  in a) 2D and b) 3D space

For the Voronoi geometry, a large number of points was initially sampled, and the Voronoi regions for each point were constructed. The final inclusions were obtained by randomly selecting a fraction of these points, in accordance with the predefined volume fraction  $\Phi_{vol} = 0.9$ . The material parameters for the selected Voronoi regions were then assigned the inclusion parameters, as shown in Figure 11. For more detailed information on the construction of the Voronoi geometry, refer to [42].

The memory usage results, presented in Figure 12, demonstrate the stark contrast between the exponential scaling of the FFT-based method and the geometry-optimized efficiency of the SFFT approach in both 2D and 3D. For the Checkerboard and reduced Checkerboard geometries, the SFFT method significantly reduces memory consumption. On the other hand, the Voronoi and Voronoi 3D geometries exhibit exponential memory growth, similar to the FFT method. For generalized geometries like the Checkerboard 3D, the SFFT method still offers superior memory efficiency compared to the FFT baseline. More complex geometries like the Spots, Voronoi, Fibres or Voronoi 3D Geometries all show exponential memory scaling similar to the state-of-the-art FFT based Method. However, due to the redundant z-component of the Fibres geometry, we still see a considerable memory reduction in comparison to the FFT-based method.

Regarding iteration times, as shown in Figure 13, we observe that the FFT method is faster for lower discretization orders. However, for the from the Checkerboard derived geometries, the SFFT method starts to outperform FFT after reaching a geometry-dependent threshold. In 2D, this crossover occurs at  $n = 15$  for the Checkerboard geometry, while in 3D, the reduced Checkerboard geometry shows a crossover around  $n = 10$ . The cross over point for the

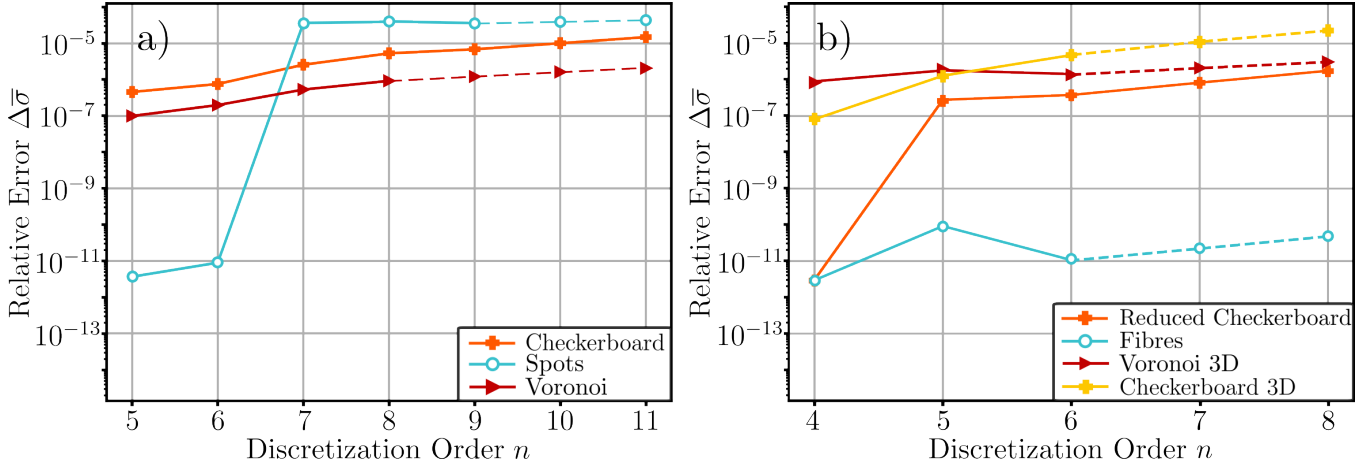


**Figure 15** Relative Error  $\Delta\bar{\sigma}$  in dependence of the discretization order  $n$  in a) 2D and b) 3D space.

Checkerboard 3D geometry is expected to be around  $n = 15$ .

In Figure 14, we see that the rank growth of the Checkerboard and all its two generalizations into 3D space exhibit sub-exponential scaling, while Voronoi, Spots and their 3D counterpart all exhibit exponential rank scaling.

Figure 15 illustrates the dependence of relative error on the discretization order  $n$ . Here, all geometries reach accuracies of  $10^{-5}$  or better.

In conclusion, these additional geometries further emphasize that the current SFFT-based Homogenization algorithm is particularly well-suited for rectangular geometries. However, the results also highlight that geometries incompatible with the existing tensor network structure exhibit scalability performance similar to that of the traditional FFT-based method.

## Appendix F Discretization Scheme

Before investigating the various geometries, it is essential to determine the most appropriate discretization scheme by analyzing the Green-Eshelby Operator. This decision is not straightforward, as the iteration time depends on multiple factors: the smoothness of the solution field (and consequently its rank), as well as the rank of the Green-Eshelby Operator itself. While more complex discretization schemes may result in smoother solution fields, they could also lead to a higher rank in the Green-Eshelby Operator, potentially impacting the efficiency of the algorithm.

To assess this, different discretization schemes - listed in Table 4 - were tested for the SFFT-based Homogenization algorithm using a Checkerboard geometry in 2D space. The rounding accuracy was set to a threshold of  $\delta_{\text{acc}} = 10^{-8}$ .

As shown in Figure 16, the staggered grid discretization outperforms all other schemes in terms of both memory usage and computational speed. However, the speed of the centered grid scheme dominates at lower discretization orders but is eventually surpassed by the staggered grid at higher orders. This result is closely tied to the strain ranks, as depicted in Figure 17 a), where the staggered grid shows lower ranks, indicating a smoother solution field.

Interestingly, Figure 17 b) reveals that the Green-Eshelby Operator in the centered grid scheme actually has a lower rank than the staggered grid over the range of discretization orders  $n$  considered. However, the staggered grid scheme seems to eventually surpasses the centered grid at higher discretization orders due to its improved scaling behaviour.

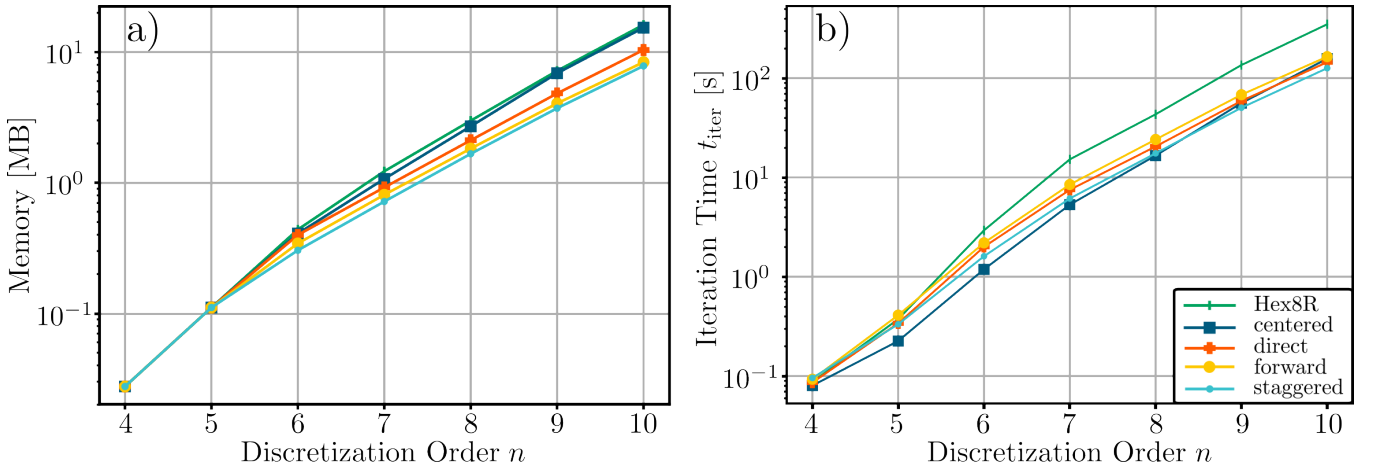


**Figure 16** a) Maximal memory used for storing the local strain and b) average iteration time  $t_{\text{iter}}$  in dependence of the discretization order  $n$ .

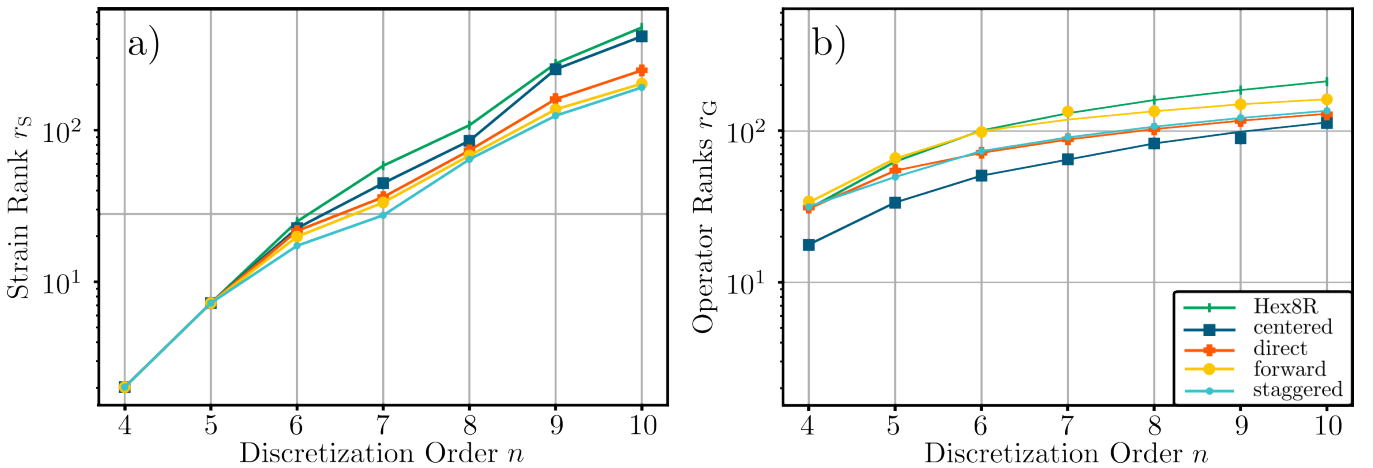


**Figure 17** a) Maximal local strain rank  $r_s$  during the evaluation of the algorithm and b) Green-Eshelby operator rank  $r_G$  in dependence of the discretization order  $n$ .